

## Original Article

**Cite this article:** Wang J-X, Zhang K-X, Windley BF, Song B-W, Kou X-H, Wang S-D, and Wang L-J (2020) A mid-Palaeozoic ocean–continent transition in the Mazongshan subduction–accretion complex, Beishan, NW China: new structural, chemical and age data constrain the petrogenesis and tectonic evolution. *Geological Magazine* **157**: 1877–1897. <https://doi.org/10.1017/S0016756820000114>

Received: 9 September 2019

Revised: 15 January 2020

Accepted: 29 January 2020

First published online: 21 April 2020


**Keywords:**

subduction–accretion mélange; magmatic arcs; Beishan accretionary collage; Central Asian Orogenic Belt

**Author for correspondence:** K.-X. Zhang,

Email: [kx\\_zhang@cug.edu.cn](mailto:kx_zhang@cug.edu.cn)

# A mid-Palaeozoic ocean–continent transition in the Mazongshan subduction–accretion complex, Beishan, NW China: new structural, chemical and age data constrain the petrogenesis and tectonic evolution

J.-X. Wang<sup>1,2</sup>, K.-X. Zhang<sup>1,2,3</sup> , Brian F. Windley<sup>4</sup>, B.-W. Song<sup>3</sup>, X.-H. Kou<sup>3</sup>, S.-D. Wang<sup>5</sup> and L.-J. Wang<sup>1,2</sup>

<sup>1</sup>School of Earth Sciences, China University of Geosciences, Wuhan 430074, China; <sup>2</sup>State Key Laboratory of Biogeology and Environmental Geology, China University of Geosciences, Wuhan 430074, China; <sup>3</sup>Institute of Geological Survey, China University of Geosciences, Wuhan 430074, China; <sup>4</sup>Department of Geology, University of Leicester, Leicester LE1 7RH, UK and <sup>5</sup>Institute of Geophysical and Geochemical Exploration, Chinese Academy of Geological Sciences, Langfang 065000, China

**Abstract**

Accretionary orogens contain key evidence for the conversion of oceanic to continental crust. The late tectonic history and closure time of the Palaeo-Asian Ocean are recorded in the Mazongshan subduction–accretion complex in the southern Beishan margin of the Central Asian Orogenic Belt. We present new data on the structure, petrology, geochemistry and zircon U–Pb isotope ages of the Mazongshan subduction–accretion complex, which is a tectonic mélange with a block-in-matrix structure. The blocks are of serpentinized peridotite, basalt, gabbro, basaltic andesite, chert and seamount sediments within a matrix that is mainly composed of fore-arc-trench turbidites. U–Pb zircon ages of two gabbros are  $454.6 \pm 2.5$  Ma and  $434.1 \pm 3.6$  Ma, an andesite has a U–Pb zircon age of  $451.3 \pm 3.5$  Ma and a tuffaceous slate has the youngest U–Pb zircon age of  $353.6 \pm 5.1$  Ma. These new isotopic ages, combined with published data on ophiolitic mélanges from central Beishan, indicate that the subduction–accretion of Beishan in the southernmost Central Asian Orogenic Belt lasted until Late Ordovician – Early Carboniferous time. Structure and age data demonstrate that the younging direction of accretion was southwards and that the subduction zone dipped continuously to the north. Accordingly, these results record the conversion of oceanic to continental crust in the southern Beishan accretionary collage.

**1. Introduction**

Of the two types of orogens – collisional (or continent–continent collision) and accretionary (or subduction–accretion) – accretionary is the least understood (Windley, 1992; Şengör *et al.* 1993; Condie, 2007; Cawood *et al.* 2009; Xiao *et al.* 2010*a, b*). Accretionary orogens form at the sites of the subduction of oceanic lithosphere against a cratonic backstop that has not been through a Wilson cycle of events, and which will not terminate until final collision with an incoming continent. The prime extant example of an accretionary orogen is the Japanese archipelago (500 Ma to present), on which our current understanding of this type of orogenesis is founded. The synthesis–culmination publications of Isozaki (1996) and Maruyama (1997) were based on more than a decade of earlier research by many Japanese geologists. Another example is the Central Asian Orogenic Belt (CAOB; 1.1 Ga to 250 Ma) (Jahn *et al.* 2000; Windley *et al.* 2007; Safonova *et al.* 2011; Wakita *et al.* 2013), which occupies the bulk of eastern–central Asia (Schulmann & Paterson, 2011), and to which the Beishan collage belongs (Xiao *et al.* 2004, 2009, 2010*c*; Tian *et al.* 2016). The southern part of the CAOB is widely referred to as the Altai (Şengör *et al.* 1993, 2014; Wilhem *et al.* 2012). The CAOB is made up of accreted prisms, mélanges, island arcs with fore-arcs and back-arcs, ophiolitic remnants that are different from the Penrose-type ophiolites in the Mediterranean (Anonymous, 1972), subducted mid-oceanic ridges and slab windows (Windley & Xiao, 2018), oceanic plateaus, major oroclinal (Xiao *et al.* 2015), ocean plate stratigraphy (Kusky *et al.* 2013; Safonova & Santosh, 2014) and old continental blocks. Palaeomagnetic and palaeogeographic relations show that the southern margin of the Siberian Plate was surrounded by the Palaeo-Asian Ocean during Neoproterozoic–Palaeozoic time (Fig. 1*a*; Wan & Zhu, 2011). Subduction of this ocean led to formation of the CAOB and the Beishan collage, and the terminal collision with the North China Craton.

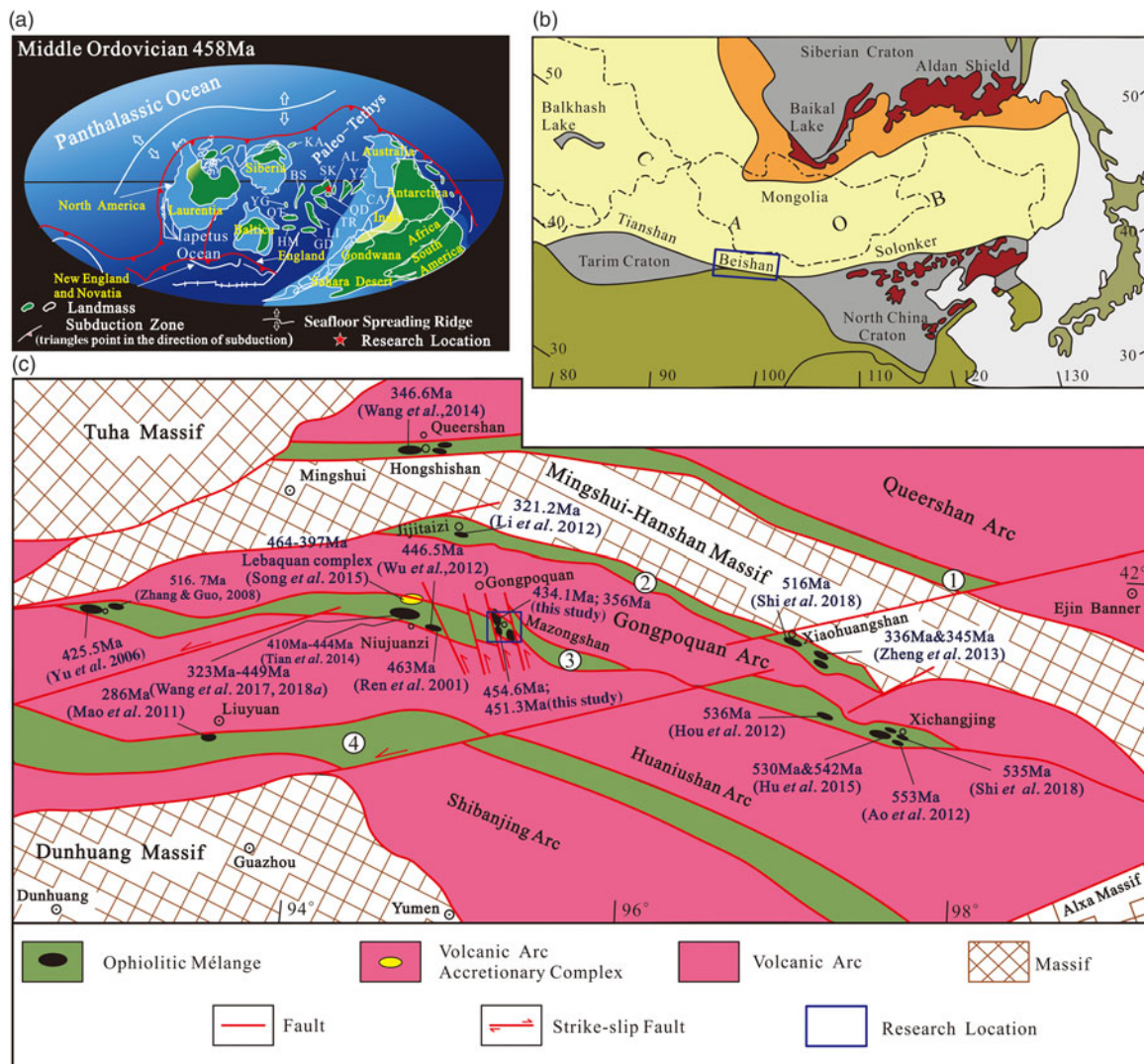


**Fig. 1.** (a) Palaeocontinental reconstruction of the globe during the Middle Ordovician Epoch (458 Ma), showing the distribution for the Middle Ordovician ocean and continent (after Wan & Zhu, 2011). AL – Alxa–Dunhuang; BS – Baoshan–Sibunasu; CA – Cathaysian; GD – Gangdise; HM – Himalayan; JG – Juggar; KD – East Kunlun; KZ – Kazakhstan; LI – Lincang–Indochina; QD – Qaidam; QT – Qiangtang; SK – Sino–Korean; TR – Tarim; YG – Yagen; YZ – Yangtze. (b) Location of the study area in the southern Altaid orogen (after Xiao *et al.* 2003; Guo *et al.* 2014). (c) Diagram showing the boundaries of tectonic units in the Beishan accretionary collage (modified by Wang *et al.* 2017): 1, Hongshishan Ophiolitic mélangé; 2, Jijitai Ophiolitic mélangé; 3, Honliuhe–Niujuanzi–Mazongshan–Xichangjing ophiolitic mélangé; 4, Liuyuan ophiolitic mélangé (Zhang & Guo, 2008; Ren *et al.* 2001; Yu *et al.* 2006; Mao *et al.* 2011; Ao *et al.* 2012; Hou *et al.* 2012; Li *et al.* 2012; Wu *et al.* 2012; Wang *et al.* 2014, 2017, 2018a; Zheng *et al.* 2013; Tian *et al.* 2014; Hu *et al.* 2015; Song *et al.* 2015; Shi *et al.* 2018).

The Beishan accretionary collage, which connects the Tianshan suture to the west with the Solonker suture to the east (Fig. 1b; Xiao *et al.* 2003), is an important component of the CAO (Xiao *et al.* 2010c; Zhang *et al.* 2015, 2016, 2018). It underwent a complex geotectonic evolution with multiple stages of subduction and accretion, but there is still much debate about its style and type of evolution: in particular, the timing of the conversions of oceanic and continental components, and of terminal collision. For example, did the CAO accretionary orogen terminate during Devonian or Carboniferous time, and was it followed by continental rifting in during Carboniferous or Permian time (Wang *et al.* 2017, 2018a) or Permian time (Xiao *et al.* 2003, 2004, 2010c; Windley *et al.* 2007)? In particular, a lack of adequate research has led to uncertainties about the structure, tectonic setting and subduction polarity of the main components in central Beishan, and this has prevented a full understanding of the entire Beishan collage (Ao *et al.* 2012, 2016; Zheng *et al.* 2013; Guo *et al.* 2014; Song *et al.* 2013a, b, c, 2014, 2015; Wang *et al.* 2017, 2018; Shi *et al.* 2018).

The centre of the Beishan accretionary collage is occupied by the Mazongshan tectonic mélangé and subduction–accretion complex (Fig. 2), which is sandwiched between the Liuyuan passive continental margin or fore-arc and the Gogonpoquan magmatic arc (Fig. 1c). Our aim in this paper is to present new detailed information about the structural relations and geochemical–isotopic data of the main components of the Mazongshan complex in order to constrain the tectonic setting, time of formation and accretionary history of the Beishan collage.

## 2. Geological background

The Beishan collage is a composite accretionary complex that is composed of fragments of island arcs, oceanic crustal debris, trench slope turbidites, and pelagic and fore-arc sediments (Xiao *et al.* 2010c; Mao *et al.* 2011; He *et al.* 2014a, b; Song *et al.* 2015; Tian *et al.* 2016; Wang *et al.* 2017). From south to north the Beishan collage is made up of the Dunhuang Massif, the Shibanjing arc, the Liuyuan ophiolitic mélangé,

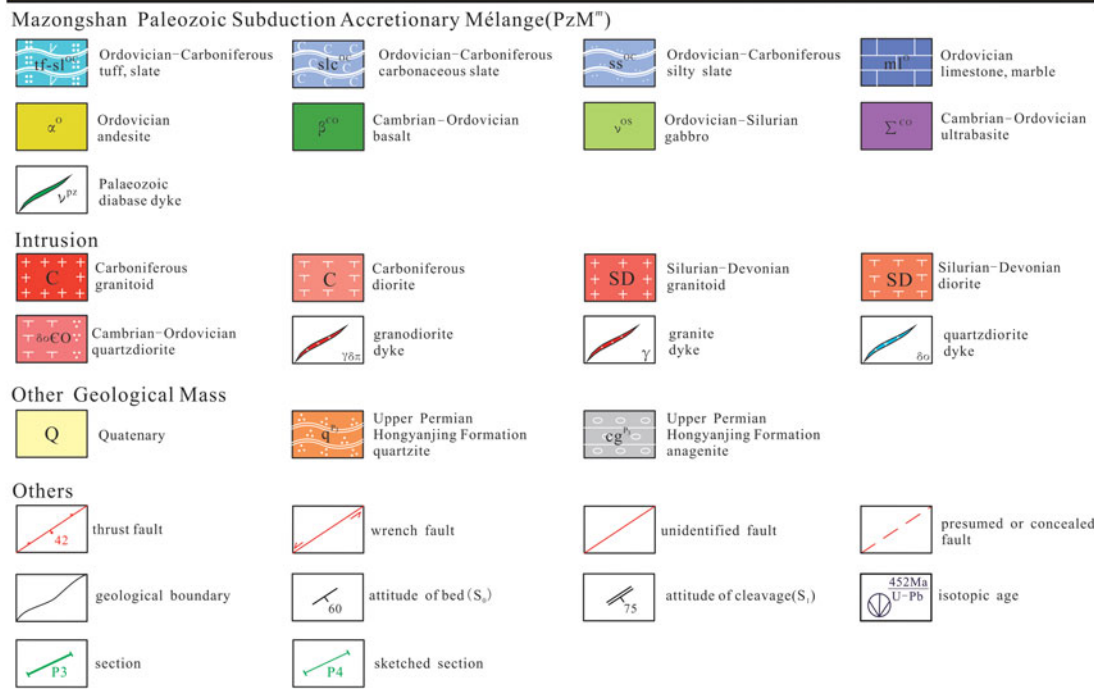
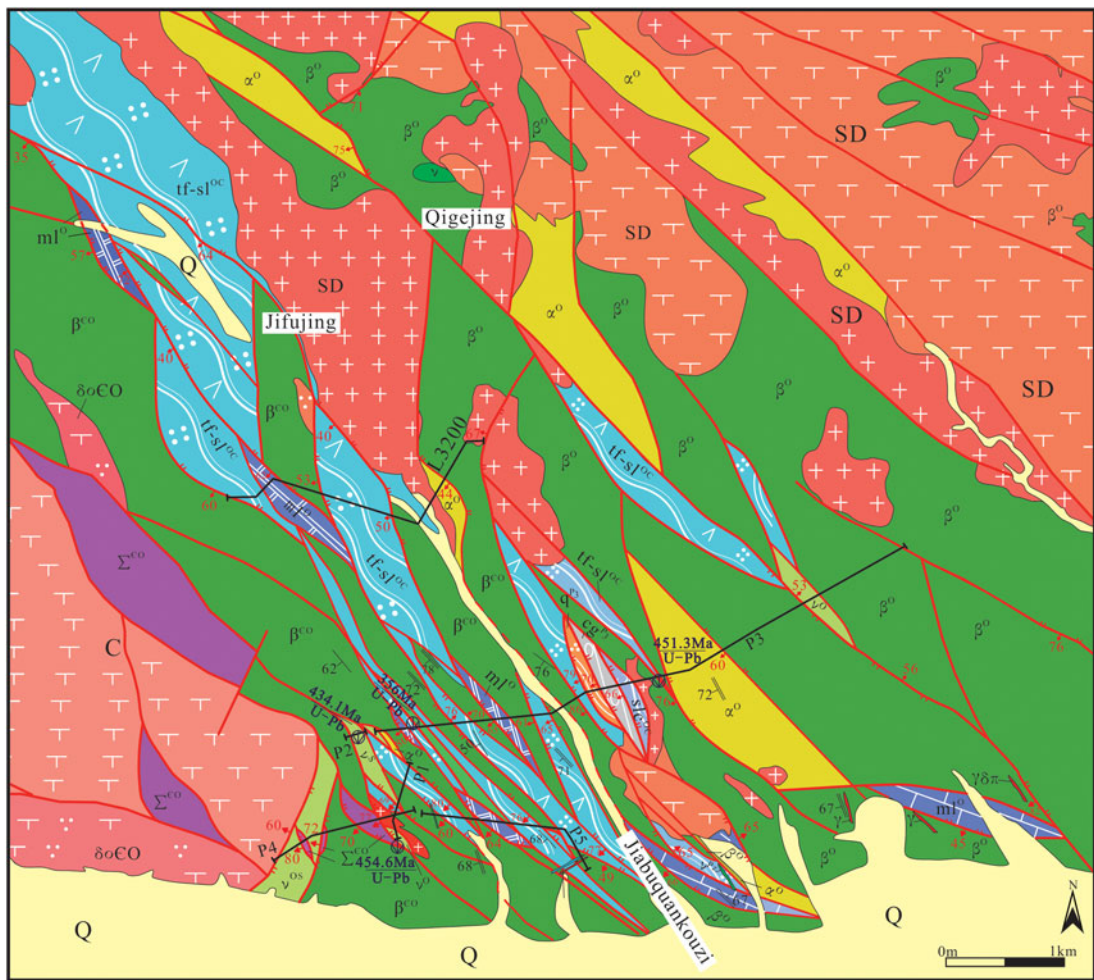


Fig. 2. Geological map of the research location (modified from the Gangu Survey Institute, 2008).

the Huaniushan arc, the Hongliuhe-Niujuanzi-Mazongshan-Xichangjing ophiolitic mélange, the Gongpoquan magmatic arc, the Jijitai-Xiaohuangshan ophiolitic mélange, the Mingshui-Hanshan continental massif, the Hongshishan ophiolitic mélange, and the Queershan arc (Fig. 1c) (Xiao *et al.* 2010c; Mao *et al.* 2011; Zhang *et al.* 2014a, b, 2016, 2018; Wang *et al.* 2017).

Stratas in the Beishan collage include Proterozoic, Palaeozoic, Mesozoic and Cenozoic. In southern Mazongshan glaciers deposited a moraine conglomerate seen in the Sinian Xichangjing Group, which contains limestone dropstones up to c. 3–8 cm across. Associated moraine gravels are mainly composed of limestone and siliceous dolomite, which suggests that the glacier travelled across a passive continental margin (Chen *et al.* 2017). The deposition was likely in a continental glacial environment, indicating that an ancient continent existed in the Beishan area during Neoproterozoic time. The lower Cambrian Shuangyingshan Formation contains bioclastic limestones and thin-bedded marbles indicative of a shallow-marine or coastal-sea environment. The Middle–Upper Cambrian Xishuangyingshan Formation is mainly composed of blue-grey pelagic cherts with thin interbeds of limestone, which may have been related to a contemporary mid-ocean-ridge basalt (MORB-) type of ophiolite in central Beishan (Shi *et al.* 2018).

The Hongliuhe–Niujuanzi–Mazongshan–Xichangjing (HNMX) ophiolitic mélange, situated in central parts of the Beishan collage, is mainly composed of Cambrian–Silurian clastic and pyroclastic rocks, many tectonic slices of ophiolitic rocks, and Carboniferous–Permian conglomerates, graywackes, tuffaceous siltstones, slates, cherts and minor limestones (Zuo *et al.* 2003; Xiao *et al.* 2014; Wang *et al.* 2017, 2018a). All these rocks are mutually juxtaposed by thrusts. From west to east along this ophiolitic mélange, there are major fault-bounded bodies of ophiolite in the Hongliuhe, Niujuanzi and Xichangjing areas. There are much geochemical data and high-resolution geochronology of these ophiolitic mélanges (Fig. 1c; Ren *et al.* 2001; Yu *et al.* 2006; Zhang & Guo, 2008; Ao *et al.* 2012; Hou *et al.* 2012; Tian *et al.* 2014; Hu *et al.* 2015; Wang *et al.* 2017; Shi *et al.* 2018), which have improved our understanding of their tectonic settings. Recently, it was reported that the youngest age from the matrix of a greywacke turbidite in the HNMX ophiolitic mélange has a Carboniferous U–Pb zircon age of 323 Ma (Wang *et al.* 2018a). Tian *et al.* (2016) reported that intrusive granodiorite was dated as Carboniferous with an age of  $308.1 \pm 3.8$  Ma from the Pochenshan area from a post-orogenic continental rift. These ages mean that the ocean that gave rise to the HNMX ophiolitic mélange was in existence from the early Cambrian to the late Carboniferous period.

The Gongpoquan Arc to the north of the HNMX ophiolitic mélange comprises Ordovician–Silurian rhyolite, rhyolitic volcanic breccia, altered andesite, feldspathic sandstone, quartzite, schist and marble, containing Silurian conodonts such as *Amarphgnathrs* sp., *A. amorphognthiform*, *A. holodontiform*, *A. tetraprionidiform*, *Parathlgnathusobesus* and *Spathognathodusprimus* (Zuo *et al.* 1994). Recently, more and more published isotopic age data indicate that the northern Gongpoquan arc formed during Ordovician–Middle Devonian time (Song *et al.* 2013b, 2014, 2015; Wang *et al.* 2016, 2018b), and this arc was the product of the northwards subduction of the Palaeo-ocean (Ao *et al.* 2012; Song *et al.* 2014, 2015). Further south, the Shuangyingshan–Huaniushan Arc developed to the south of the HNMX ophiolitic mélange. The subduction-related plutons in the Huaniushan Arc are Silurian–Late Devonian in age ( $373.8 \pm 1.6$  to  $424.0 \pm 1.3$  Ma; Mao *et al.*

2012; Ding *et al.* 2015). Xiao *et al.* (2010c) proposed that the Shuangyingshan–Huaniushan Arc developed during Ordovician–Carboniferous time.

The Mazongshan complex was earlier thought to be Precambrian–Cambrian in age because of its pervasive metamorphic and deformational fabrics (Gangu Survey Institute, 2001), but it was then found to be Ordovician in age and connected to the Lebaquan arc–fore-arc complex (Gangu Survey Institute, 2008). Today, the field relations, geochemical characteristics and tectonic setting of the Mazongshan complex are controversial: alternatives are an arc, continental margin rift, an arc–fore-arc or an ophiolitic mélange (Fig. 1c) (Gangu Survey Institute, 2001; Song *et al.* 2013a, b, 2014, 2015; Xiao *et al.* 2014).

### 3. Structure, lithology and petrography of the Mazongshan complex

#### 3.a. Field relations

We recently carried out detailed field-based structural mapping and sample collections in central Beishan, mainly in the Jiabuquankouzi area and the associated Lebaquan complex. The Mazongshan complex, which is well exposed from the south of Jiabuquankouzi to the north of Qigejing (Fig. 2), comprises diverse blocks up to c. 120 m across of seamount sediments, serpentinized peridotite, gabbro, basalt, andesite and chert in a turbiditic slaty matrix (Fig. 3a–c, e). These variably deformed rocks are thrust-imblicated and strongly sheared. The many blocks behaved competently within the ductile, tightly folded, slaty matrix. The lithologies and structures of the Mazongshan complex are characteristic of a subduction–accretion mélange.

The thickest P3 cross-section (Fig. 4) contains (from bottom to top): greenish amygdaloidal and vesicular basalts; black-green, poorly exposed, serpentinized peridotites (see the eastern side of the P3 cross-section); and cumulate layered and graded, but noticeably inverted, gabbros (on the western side of the P3 cross-section). Another type of basalt that is uniquely associated with marbles mainly crops out on the western side of the P3–P5 cross-section. These successions are more than 20 m thick, comprising lower grey basalts and upper reddish marbles (Fig. 4a, b).

The matrix of the mélange is mainly composed of tuffaceous and silty slates, which contain innumerable tectonic lenses and blocks of gabbro, basalt and serpentinized peridotite c. 0.5–150 m long. All have been broken into fragments by reverse faults.

The Lebaquan arc–fore-arc, which is tens of kilometres from the Mazongshan complex (Song *et al.* 2014, 2015), is mainly composed of metasedimentary quartzite, phyllite, chlorite–quartz schist, sericite–quartz schist, chert, marble and mafic volcanic rocks, plus gneissic granite plutons and later leucogranite–pegmatites and mafic dykes. Clearly, the Mazongshan complex is very different from the Lebaquan complex in terms of lithologies and structures.

#### 3.b. Petrography

Ophiolitic rocks in the Mazongshan complex include serpentinized peridotite, gabbro and basalts, which are weakly altered. Serpentinized peridotite is generally composed of altered olivine (80% of rock volume), clinostattite (10%), tremolite, magnetite and spinel (Fig. 5a, b). Most basalts contain about 10% phenocrysts of plagioclase and ferromagnesian minerals within a 90% matrix of plagioclase, chlorite, calcite, magnetite and titanite (Fig. 5c, d).

Gabbros are hypidiomorphic and consist of medium- to fine-grained plagioclase and pyroxene; some pyroxenes are partly to

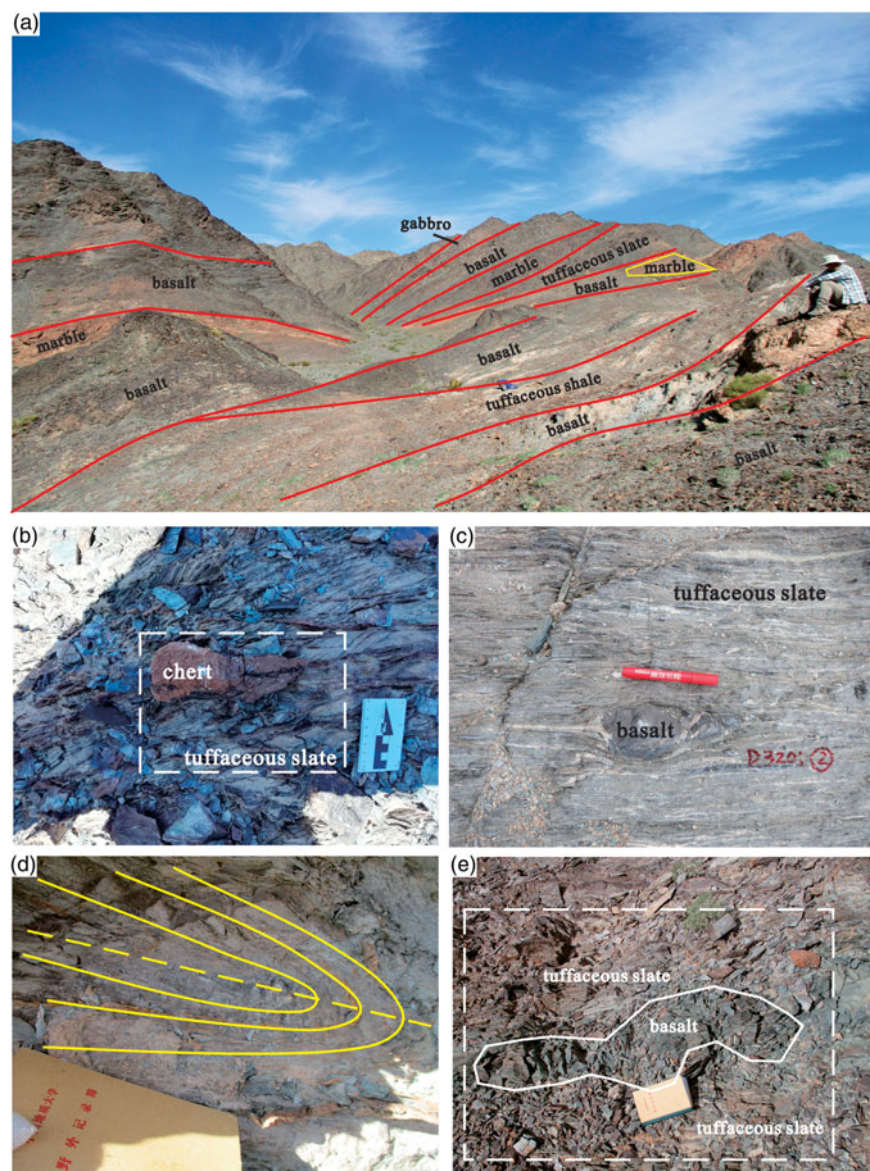


**Fig. 3.** Field photographs from the Mazongshan complex, central Beishan: (a, b, c, e) characteristic blocks in the matrix of the mélangé; and (d) tight folds in the turbidite matrix.

completely replaced by epidote, chlorite, hornblende and actinolite. Amygdaloidal andesite blocks (Fig. 5e, f) contain irregular or circular amygdalae, consisting of plagioclase, chlorite, epidote, calcite, apatite, titanite and pyrite. The ‘matrix’ of turbidites is mostly tuffaceous slate and silty slate composed of quartz phenocrysts, some of which occurs in a foliated matrix. Tuffaceous slate matrix (Fig. 5g, h) shows a directional arrangement to some extent, containing irregular or circular quartz, feldspar and mica.

#### 4. Sampling and analytical methods

Our representative samples from the mélangé of the Mazongshan complex were collected from the least-altered and least-sheared parts of most of the tectonic blocks. The samples were crushed and pulverized to 200 mesh using an agate mortar in the State Key Laboratory of Geological Processes and Mineral Resources (GPMR), China University of Geosciences, Wuhan. A total of 20 samples were analysed for major and trace elements, including two gabbros (one from cross-section 1 and one from cross-section 2), 14 samples from cross-section 3 (that include 1 serpentinized

peridotite, 3 andesites and 8 basalts), and a further 6 basalts from cross-sections 4 and 5 and line 3200. Four samples of the gabbros, andesites and tuffaceous slates were analysed for zircon U–Pb isotope analysis.

#### 4.a. Major- and trace-element analyses

To constrain the tectonic setting of the Mazongshan complex, 1 serpentinized peridotite, 11 basalts, 1 gabbro and 7 andesite samples were collected from the blocks for whole-rock major-, trace- and rare-earth-element analyses. All the sample locations are highlighted in Figure 5.

Whole-rock major-, trace- and rare-earth-element analyses were performed at the Hubei Province Geological Experimental Testing Center. Major elements were measured by X-ray fluorescence spectrometry and plasma spectrometry with a Magix-pro2440 spectrometer, for which the analytical uncertainty was better than 5%. The trace elements were analysed with a Thermochemical X7 inductively coupled plasma – mass spectrometer (ICP-MS) with analytical uncertainties of 5–10%. Methods of sample preparation, analysis

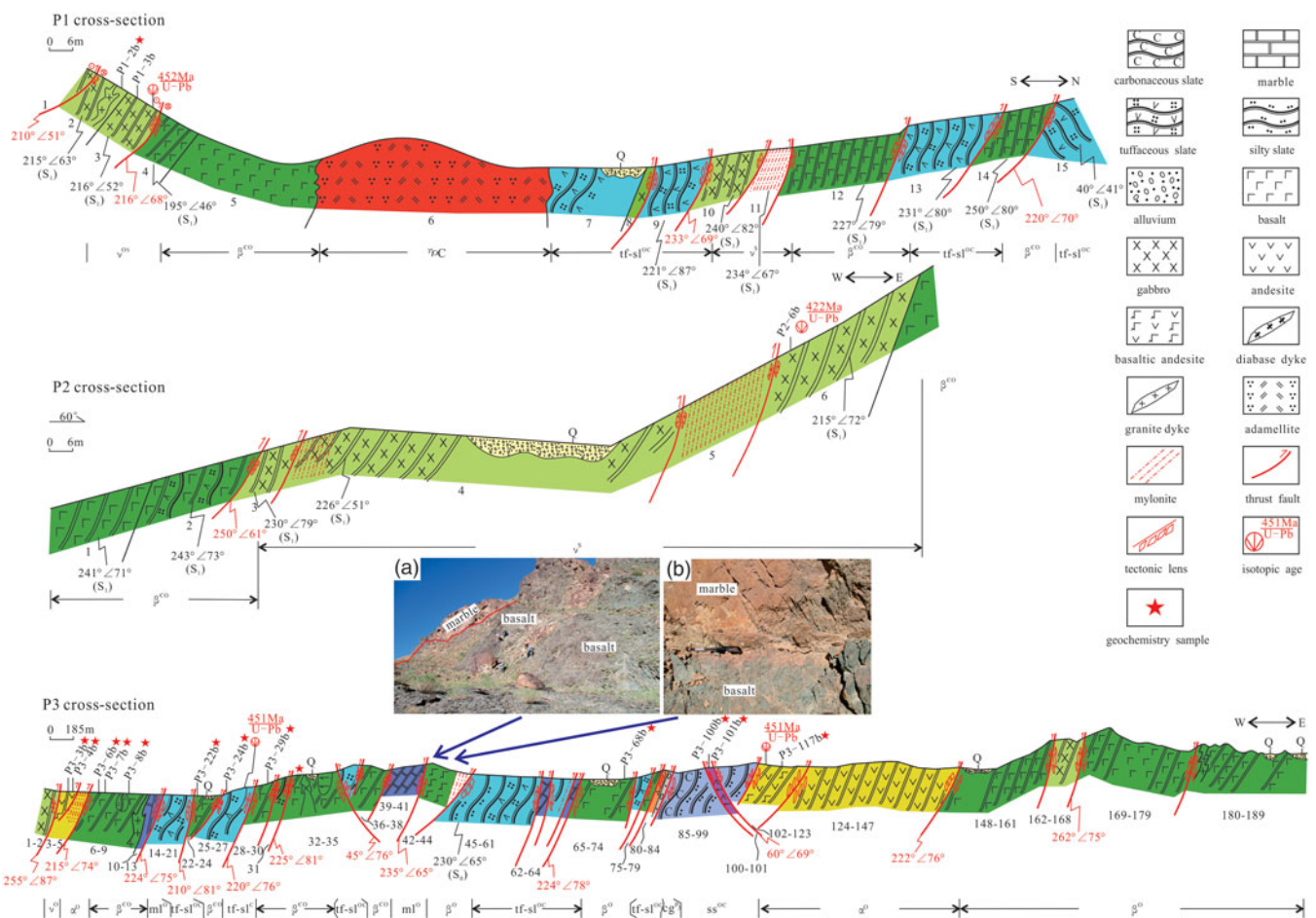


**Fig. 4.** (Colour online) Cross-sections P1, P2 and P3, showing their detailed lithologies, structural patterns and sample locations in the Jiabuquankouzi area. See Figure 2 for legend.

and processing followed the procedures of Liu *et al.* (2008). Representative major- and trace-element analyses are listed in Table 1.

#### 4.b. Zircon U–Pb isotope analysis

We attempted to collect fresh samples for dating and geochemical analyses from the Jiabuquankouzi area. Four samples (P1-3, P2-6, P3-117 and P3-27) of intermediate–basic rocks and slate were collected from the P1, P2 and P3 cross-sections (petrographic characteristics of sample P1-3, P3-117 and P3-27 are shown in Fig. 5a, b, e–h). Sample P1-3 and sample P2-6 are dark-green gabbros collected from the western side of the Jiabuquankouzi area. Sample P3-117 is yellowish-green andesite collected from the eastern side of the Jiabuquankouzi area. Sample P3-27 is light-grey tuffaceous slate collected from the central part of the Jiabuquankouzi area. These samples, which represent the typical lithology of the Mazongshan complex, constrain the evolution stages of the Mazongshan complex. All sample locations are highlighted in Figures 2 and 4.

Zircons were separated following the standard procedures of crushing and heavy liquid and magnetic techniques, and hand-picked under a binocular microscope at the Langfang Credit Geological Service Co., Hebei Province. A total of 30 grains from each sample were picked randomly, enclosed in epoxy resin and polished to approximately half their thickness. The zircons were

photographed under reflected and transmitted light, and their cathodoluminescence (CL) images were prepared at the State Key Laboratory of Geological Processes and Mineral Resources, China University of Geosciences, Wuhan, China. Zircon U–Pb dating was undertaken with an Agilent7500a ICP-MS instrument. Zircon91500 was used as an external standard for the U–Pb dating, and U, Th and Pb concentrations were calibrated using  $^{29}\text{Si}$  as an internal standard and NIST 610 as a reference material. The typical instrument operating conditions followed those reported in Liu *et al.* (2008). All data were acquired from the zircons in single spot ablation mode with a spot size of 32  $\mu\text{m}$ . Every analysis from each sample incorporated one background acquisition lasting 20–30 s followed by 50 s of data acquisition. Offline selection and integration of background and analytical signals, time-drift corrections and quantitative calibrations for trace-element analyses and U–Pb dating were made with an ICP-MS Data Cal ver. 9. (Liu *et al.* 2008), and concordia diagrams were prepared and weighted mean calculations performed using Isoplot3 software (Ludwig, 2000).

## 5. Analytical results

### 5.a. Major and trace elements

The major elements were normalized based on the values in Table 1 to 100% excluding loss on ignition (LOI). Some samples from the Mazongshan complex show high LOI (up to 7.99 wt%

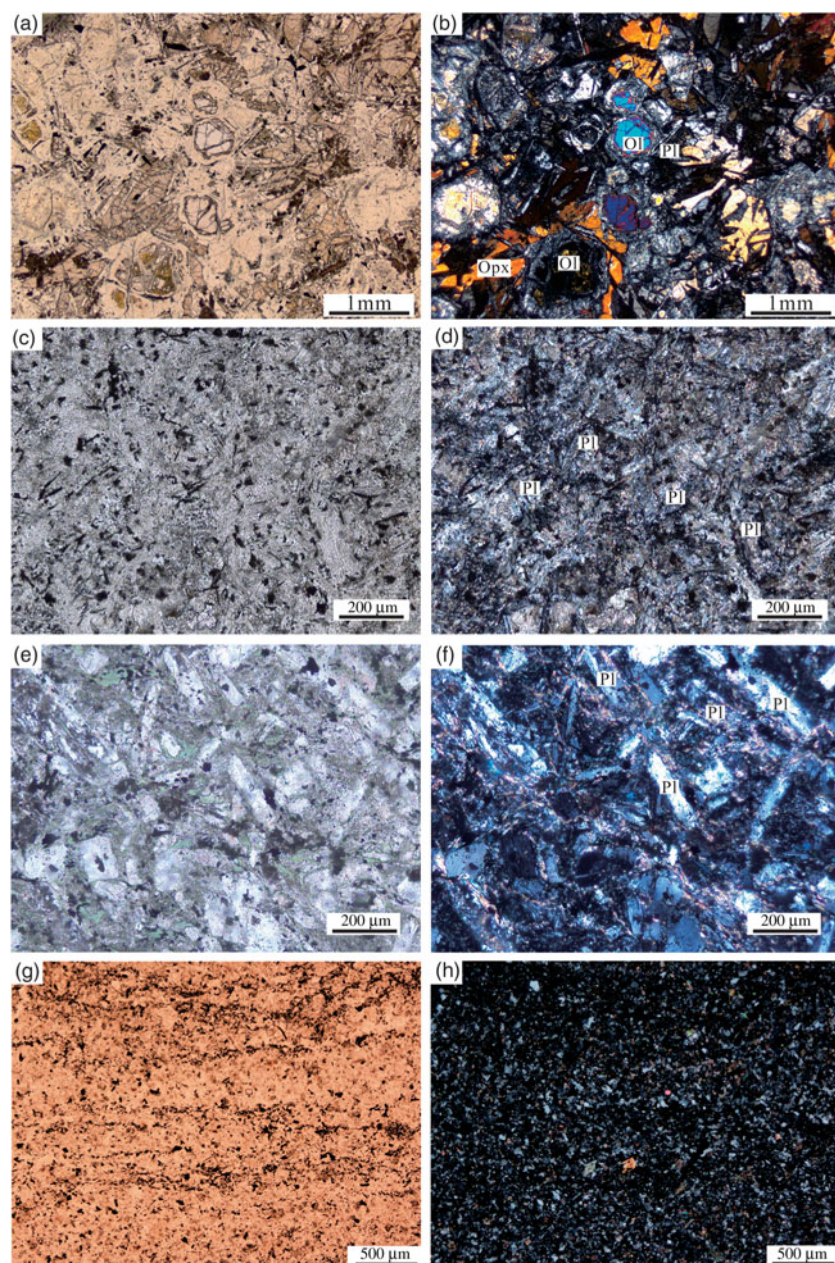


**Fig. 5.** Photomicrographs of petrographic features of the Mazongshan complex, Beishan: (a, b) serpentinized peridotite; (c, d) metabasalt; (e, f) andesite; and (g, h) tuffaceous slate. Ol - olivine; Pl - plagioclase; Opx - clinoenstatite.

for gabbro), indicating different degrees of alteration. Alteration may lead to the migration of some active elements, such as most of the major elements and low-ion lithophile elements (LILEs), but trace elements Zr, Nb, Y and rare earth elements (REEs) Th and Ta are relatively stable. In this study we only used the relatively stable elements mentioned above to determine the lithology, genesis and tectonic settings. On the basis of their geochemical and field characteristics, samples mainly comprised basalts and andesites.

Basalt samples have large variations in contents of  $\text{SiO}_2$  (51.21–53.80 wt%),  $\text{MgO}$  (4.02–7.42 wt%),  $\text{TiO}_2$  (0.87–1.86 wt%),  $\text{Na}_2\text{O}$  (2.09–4.87 wt%),  $\text{Mg no.}$  (42.02–62.92) (where  $\text{Mg no.}$  is defined as  $100 \times \text{Mg}^{2+}/(\text{Mg}^{2+} + \text{Fe}^{2+} + \text{Fe}^{3+})$ ). These samples are high in  $\text{Al}_2\text{O}_3$  (16.14–21.42 wt%),  $\text{FeO}^{\text{I}}$  (7.82–10.23 wt%) and  $\text{CaO}$  (1.08–10.43 wt%), and  $\text{K}_2\text{O}/\text{Na}_2\text{O}$  ratios range from 0.01 to 0.42. On a Nb/Y versus (v.) Zr/ $\text{TiO}_2$  diagram (Fig. 6), they plot

in the basalt and andesitic basalt fields. The samples are relatively enriched in light REEs (LREEs) ( $\text{La}/\text{Yb}_{\text{cn}} = 1.28\text{--}6.38$ ,  $\text{La}/\text{Sm}_{\text{cn}} = 0.86\text{--}2.6$ ) and differentiated in heavy REEs (HREEs) ( $\text{Gd}/\text{Yb}_{\text{cn}} = 1.25\text{--}1.71$ ). Europium ( $\text{Eu}/\text{Eu}^* = 0.65\text{--}1.04$ ) anomalies are weakly negative to positive.

All of the seven andesite samples contain  $\text{SiO}_2$  (54.47–59.75 wt%),  $\text{Na}_2\text{O}$  (3.61–5.78 wt%),  $\text{TiO}_2$  (1.02–3.25 wt%) and  $\text{FeO}^{\text{I}}$  (6.55–12.53 wt%). On chondrite-normalized diagrams (Fig. 7c), they are clearly enriched in LREE ( $\text{La}/\text{Yb}_{\text{cn}} = 3.81\text{--}11.26$ ) and depleted in HREE ( $\text{Gd}/\text{Yb}_{\text{cn}} = 1.43\text{--}1.81$ ). Europium ( $\text{Eu}/\text{Eu}^* = 0.57\text{--}0.87$ ) anomalies are markedly negative.

The serpentinized peridotite (P3-100) sample has a relatively high  $\text{MgO}$  content (23.29 wt%) and low  $\text{Al}_2\text{O}_3$  (10.76 wt%) and  $\text{Na}_2\text{O}$  (0.87 wt%) contents. The geochemical characteristics of the gabbro sample are similar to those of the basalts in being characterized by 53.61 wt%  $\text{SiO}_2$ , 1.68 wt%  $\text{K}_2\text{O}$ , 3.70 wt%  $\text{Na}_2\text{O}$  and

**Table 1.** Major and trace element composition for the Mazongshan complex

Sample no.	P1-2	P3-6	P3-7	P3-8	P3-29	P3-32	P3-101	P4-1	P4-2	P4-7	P5-21	D3200	P3-3	P3-4	P3-22	P3-24	P3-68	P3-117	P4-8	P3-100	
Lithology	Gabbro	Basalts											Andesite						Serpentinized peridotite		
Oxides (wt %)																					
SiO <sub>2</sub>	48.83	48.53	50.32	49.56	49.07	50.16	49.62	49.87	52.23	52.20	50.33	49.85	52.18	51.71	50.98	55.25	54.39	56.96	56.83	43.94	
TiO <sub>2</sub>	1.22	0.94	1.04	0.92	1.54	1.34	1.67	1.34	1.61	0.84	1.76	0.96	0.96	1.01	3.04	2.50	1.30	1.74	1.34	0.67	
Al <sub>2</sub> O <sub>3</sub>	15.64	19.21	18.00	17.28	18.33	16.81	16.64	18.03	16.89	16.14	20.21	20.49	17.14	18.53	13.45	13.47	19.72	14.22	16.15	9.94	
FeO	6.32	6.52	4.95	5.12	7.72	6.18	6.45	6.15	5.42	5.25	6.18	6.05	5.70	5.85	6.75	5.65	4.15	4.58	4.05	6.75	
Fe <sub>2</sub> O <sub>3</sub>	3.22	2.60	5.04	4.28	2.23	2.64	1.31	4.14	4.82	3.82	1.41	3.26	3.67	3.86	4.76	7.18	2.33	4.11	3.55	2.26	
MnO	0.07	0.16	0.18	0.14	0.09	0.07	0.16	0.11	0.11	0.09	0.06	0.14	0.12	0.13	0.18	0.14	0.04	0.17	0.08	0.15	
MgO	3.99	4.67	4.49	4.34	6.46	4.35	7.19	5.30	3.93	5.77	6.78	4.73	5.43	5.30	3.67	2.35	5.86	2.98	3.42	21.50	
CaO	6.64	8.13	7.80	6.25	4.71	6.96	10.10	6.81	7.27	7.85	1.02	6.55	2.99	2.82	5.32	3.32	0.71	4.09	7.02	6.10	
Na <sub>2</sub> O	3.37	2.23	3.54	3.63	3.43	4.10	3.08	3.60	3.87	3.69	4.60	1.98	5.44	4.71	4.41	3.76	4.45	3.62	3.52	0.81	
K <sub>2</sub> O	1.53	0.44	0.02	1.00	0.43	0.44	0.48	1.07	1.15	1.21	1.94	0.51	0.23	0.76	0.24	1.98	2.16	2.31	1.28	0.13	
P <sub>2</sub> O <sub>5</sub>	0.26	0.19	0.19	0.17	0.18	0.18	0.19	0.24	0.35	0.16	0.22	0.20	0.28	0.25	0.67	1.07	0.30	0.55	0.40	0.08	
LOI	7.99	5.31	3.62	6.62	4.74	6.08	2.14	2.42	1.53	2.15	4.54	4.33	5.22	4.40	5.85	2.69	3.94	4.05	1.64	6.41	
Total	99.08	98.93	99.19	99.31	98.94	99.31	99.03	99.09	99.17	99.19	99.06	99.05	99.36	99.33	99.32	99.36	99.35	99.38	99.30	98.74	
Mg no.	43.79	48.69	46.00	46.54	54.44	47.78	62.92	49.15	42.02	54.44	62.10	48.64	52.05	50.57	37.45	25.88	62.80	39.32	45.97	81.51	
REE (ppm)																					
La	12.09	10.72	12.38	8.14	9.65	13.08	6.40	18.45	17.87	16.13	13.02	12.00	12.80	14.27	39.93	65.41	24.41	33.56	23.22	2.00	
Ce	25.26	20.05	21.35	16.56	19.78	27.17	17.65	25.26	42.34	35.35	25.51	23.50	25.18	27.34	89.06	143.86	47.69	76.27	53.13	5.45	
Pr	3.64	3.32	3.59	2.47	3.21	3.84	3.15	5.15	6.74	5.31	3.90	3.17	3.35	3.72	11.94	19.64	5.90	10.29	7.71	1.09	
Nd	17.00	15.48	16.50	11.04	14.68	16.48	15.53	22.25	32.41	25.97	16.81	13.21	14.08	15.69	50.31	82.50	21.76	42.19	36.23	5.52	
Sm	4.11	3.59	3.63	2.94	3.53	4.12	4.79	4.58	7.77	6.96	3.48	3.19	3.38	3.74	11.87	19.19	4.00	10.12	8.63	1.85	
Eu	0.95	1.15	1.08	0.99	1.11	1.40	1.60	1.38	2.45	1.48	0.85	1.07	0.99	1.13	2.61	3.72	0.96	2.40	2.01	0.66	
Gd	4.04	3.33	3.24	3.02	3.47	4.63	5.53	4.03	7.00	6.71	3.14	2.98	3.56	3.94	12.57	20.29	3.39	10.89	7.75	2.19	
Tb	0.79	0.58	0.59	0.50	0.65	0.78	0.99	0.72	1.26	1.24	0.60	0.49	0.57	0.63	2.03	3.28	0.52	1.80	1.38	0.43	
Dy	5.28	3.58	3.57	3.03	4.16	4.74	6.66	4.28	7.49	7.89	3.81	2.88	3.51	3.69	12.04	19.41	2.71	10.93	8.45	2.70	
Ho	1.08	0.71	0.68	0.63	0.81	0.95	1.42	0.84	1.49	1.61	0.77	0.60	0.70	0.75	2.41	3.90	0.55	2.22	1.65	0.58	

(Continued)



Table 1. (Continued)

Er	3.17	1.92	1.89	1.77	2.20	2.70	3.94	2.36	4.24	4.64	2.25	1.66	1.96	2.13	6.87	11.14	1.56	6.48	4.63	1.65
Tm	0.49	0.29	0.28	0.25	0.34	0.39	0.58	0.36	0.64	0.70	0.35	0.25	0.30	0.33	1.01	1.63	0.23	1.01	0.69	0.24
Yb	2.84	1.61	1.59	1.52	1.93	2.37	3.58	2.07	3.74	4.19	2.07	1.56	1.85	2.03	6.16	9.98	1.56	6.32	3.92	1.51
Lu	0.48	0.26	0.26	0.22	0.29	0.35	0.51	0.35	0.67	0.73	0.37	0.23	0.28	0.30	0.94	1.51	0.24	1.00	0.67	0.24
ΣREE	81.23	66.58	70.63	53.09	65.81	83.00	72.33	92.09	136.12	118.91	76.95	66.78	72.49	79.69	249.75	405.46	115.48	215.48	160.04	26.11
Trace elements (ppm)																				
Sc	33.11	32.13	35.68	33.08	17.01	23.41	40.64	34.76	30.66	40.76	33.92	29.26	27.35	29.12	32.31	24.48	27.58	17.93	27.02	23.76
V	310.60	265.50	291.10	243.65	183.30	209.66	231.48	288.59	259.48	202.36	219.98	270.46	204.53	213.40	292.51	154.68	183.15	142.46	184.93	113.80
Cr	44.06	73.42	71.56	40.81	90.82	39.38	240.27	77.77	40.68	139.20	394.16	48.45	90.50	63.16	26.25	1.49	101.73	13.13	71.58	2651.72
Co	31.52	29.17	32.31	32.40	44.81	33.92	34.68	25.63	22.79	23.54	36.38	28.90	31.34	31.27	29.03	30.22	21.94	17.12	16.40	76.41
Ni	11.23	23.38	15.69	16.20	62.74	36.10	98.38	13.27	12.86	37.99	87.62	17.89	46.71	34.23	13.71	1.41	40.82	4.14	20.64	884.40
Rb	38.91	11.04	2.06	28.74	9.17	12.02	29.29	35.06	33.58	34.22	65.93	13.14	6.99	20.05	8.14	45.59	64.94	54.58	45.01	6.16
Sr	125.58	478.27	680.03	301.43	295.36	273.04	231.15	366.44	379.03	345.71	130.55	655.35	227.67	363.42	153.80	131.06	75.82	117.24	450.08	99.77
Y	24.75	16.14	15.82	15.00	18.60	23.96	36.48	20.12	34.12	37.03	16.16	14.68	16.99	18.33	61.43	101.66	11.43	57.88	38.52	14.55
Zr	89.86	54.91	56.26	54.95	98.98	128.11	144.65	80.35	92.06	62.78	194.30	69.78	77.72	88.01	416.69	722.70	165.72	431.64	248.06	47.33
Nb	4.84	2.04	2.28	3.12	2.41	3.41	3.98	3.96	6.85	6.60	3.01	5.04	4.11	5.78	12.42	17.54	6.47	13.10	8.68	0.74
Ta	0.19	0.13	0.15	0.49	0.16	0.41	2.03	0.22	0.38	0.37	0.20	1.10	0.48	0.83	1.10	1.41	1.30	0.95	0.38	1.28
Cs	0.98	0.66	0.21	1.32	0.41	0.31	5.17	0.87	0.90	0.71	1.93	1.13	0.23	0.67	0.07	1.43	3.51	0.78	0.57	8.07
Ba	202.09	187.70	75.32	289.81	93.85	75.93	297.43	254.84	302.91	307.38	248.85	384.26	106.94	233.88	159.35	631.92	214.81	782.71	301.90	98.60
Hf	2.38	1.58	1.67	2.10	2.90	3.70	3.74	1.94	2.55	1.58	4.93	1.91	2.40	2.90	9.80	17.60	4.15	10.30	7.04	1.16
Pb	4.54	11.40	13.92	6.23	2.23	2.58	2.34	1.85	2.57	3.67	3.06	10.68	7.46	9.68	5.13	2.89	2.85	110.00	2.22	1.74
Th	3.36	1.69	1.88	1.73	1.27	3.25	2.89	1.04	3.22	2.40	11.36	3.69	2.42	2.94	11.87	21.21	4.70	7.07	2.54	0.29
U	1.91	0.58	0.64	0.61	0.28	0.75	0.50	0.73	3.16	1.23	1.66	0.84	0.76	0.83	3.47	5.59	1.01	2.15	1.82	0.13

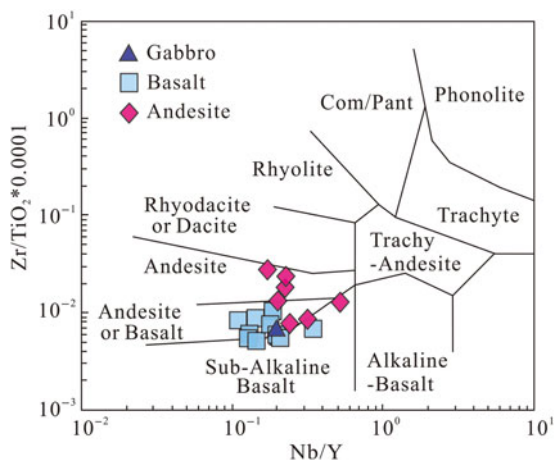


**Fig. 6.** (Colour online) Nb/Y v. Zr/Ti diagram of volcanic rocks from the Mazongshan complex (after Winchester & Floyd, 1977). Triangles, gabbro; squares, basalt; diamonds, andesite.

4.38 wt% MgO. The gabbro sample displays enriched LREE ( $\text{La}/\text{Yb}_{\text{cn}} = 3.05$ ) and less differentiated HREE ( $\text{Gd}/\text{Yb}_{\text{cn}} = 1.18$ ).

### 5.b. Geochronology

The size of zircon grains in the cumulate gabbro (sample P1-3) ranges from 80 to 200  $\mu\text{m}$ . Most zircon grains have columnar or irregular shapes, and a few have cracks. The CL images (Fig. 8a) display a complex structure. Some grains have clear oscillatory zones of magmatic origin, while others have bright–dark bands or no obvious oscillatory zones. Of the 30 analysed spots, 26 yielded concordant ages; their Th contents ranged from 124.8 to 1378.6 ppm, their U contents from 268.8 to 1148.8 ppm, and their Th/U ratios from 0.4 to 1.2. The Th/U ratio of magmatic zircons is greater than 0.3; the zircons of sample P1-3 are therefore typically magmatic. The ages ranged from 453.8 to 455.6 Ma (Fig. 9a) and yield a weighted mean  $^{206}\text{Pb}/^{238}\text{U}$  age of  $454.6 \pm 2.5$  Ma (mean square weighted deviation (MSWD) = 0.007), which we interpret to be the time of crystallization of the cumulate gabbro block (Fig. 9b; see Table 2 for more details on data sources).

The zircon grains of gabbro sample P2-6 are relatively small, of the order of 50–150  $\mu\text{m}$ . Most grains are euhedral and prismatic and their length/width ratios range from 1.5 to 3. Sample P2-6 contains two zircon types, illustrated by their CL images (Fig. 8b). Most grains have magmatic oscillatory zones of different lengths and widths, but a few have cores with obvious magmatic oscillatory zones. A total of 18 concordant ages were obtained from sample P2-6, but the  $^{206}\text{Pb}/^{238}\text{U}$  age of point 4 is  $652 \pm 7$  Ma, which is inconsistent with the overall age; this grain was likely inherited from a crustal component of the gabbro source or was captured during magmatic emplacement. The Th contents of the 18 zircons range from 77.9 to 1470.4 ppm, the U contents from 113.5 to 608.6 ppm, and the Th/U ratios from 0.2 to 2.4; these values suggest that the zircons from this gabbro had a magmatic origin. The ages range from 433.5 to 435.3 Ma (Fig. 9c) and yield a weighted mean  $^{206}\text{Pb}/^{238}\text{U}$  age of  $434.1 \pm 3.6$  Ma (MSWD = 0.0077), which we interpret as the time of crystallization of the gabbro block (Fig. 9d; see Table 2 for more details on data sources).

A total of 12 zircon grains, which were analysed from meta-basaltic andesite sample P3-117, yielded concordant ages. The grains have small and complex morphologies, and their ages range

from  $445 \pm 8$  (point 7) to  $2800 \pm 31$  Ma (point 17), which implies that many are detrital zircons. According to their zircon CL images (Fig. 8c), the meta-andesite zircons are divisible into two types. One type is euhedral and prismatic, and characterized by magmatic oscillatory zones of different lengths and widths, and has no inherited zircons. The Th contents of sample P3-117 range from 86.3 to 372.9 ppm, the U contents from 131.6 to 691.5 ppm, and the Th/U ratios from 0.3 to 1.0; these values indicate that the zircons in this basaltic andesite are typically magmatic. The ages have a small range from 445.5 to 459.9 Ma, and 10 concordant ages yield a weighted mean  $^{206}\text{Pb}/^{238}\text{U}$  age of  $451.3 \pm 3.5$  Ma (MSWD = 0.93) (Fig. 10a). Other zircons are subcircular or round, and their CL images display no rhythmic bands or oscillatory zones (points 4 and 17) (Fig. 8c). The Th/U ratios of points 4 and 17 are 0.5 and 0.6, respectively. These ancient zircons may be inherited from a crustal component of the meta-andesite source. The weighted mean  $^{206}\text{Pb}/^{238}\text{U}$  age of most magmatic zircons is therefore  $451.3 \pm 3.5$  Ma (MSWD = 0.93), which we interpret as the time of crystallization of the meta-andesite block (Fig. 10b; see Table 2 for more details on data sources).

The zircon grains in the tuffaceous slate sample P3-27 range from 60 to 150  $\mu\text{m}$  in size. Most grains have columnar or irregular shapes, and a few have metamorphic edges. The CL images (Fig. 8d) clearly show complex structures. Some grains have obvious oscillating zones of magmatic type, but others have bright–dark bands or no oscillatory zones. A total of 98 spots were analysed, 54 of which yielded concordant ages. The Th contents of these 54 zircons range from 38.0 to 485.6 ppm, the U contents from 111.2 to 576.7 ppm, and the Th/U ratios from 0.3 to 0.8. The Th/U ratio of magmatic zircons is greater than 0.3; the zircons of sample P1-3 are therefore typically magmatic. The ages range from 355.1 to 374.4 Ma (Fig. 10c), and the youngest  $^{206}\text{Pb}/^{238}\text{U}$  age is  $353.6 \pm 5.1$  Ma. We interpret this youngest age to be the time of deposition of the tuffaceous pelite, which is not older than early Carboniferous (Fig. 10d; see Table 2 for more details of data sources).

## 6. Discussion

### 6.a. Age and spatial distribution of the Mazongshan complex

The times of formation of the blocks and matrix of the mélangé in the Mazongshan complex in the central Beishan accretionary collage have, so far, remained undetermined, meaning that their evolution is not well understood. Our two gabbros have U–Pb zircon ages of 454.6 and 434.1 Ma, and the basaltic andesite has a U–Pb zircon age of 451.3 Ma, that is, the mélangé formed between the Late Ordovician and early Silurian periods.

In turbidites, the youngest detrital zircon U–Pb ages can be used to determine their order depositional age limit (Brown & Gehrels, 2007; Dickinson & Gehrels, 2009). The metasedimentary rocks in this study underwent strong deformation, but the Carboniferous zircons retain clear oscillatory zones and high Th/U ratios ( $> 0.4$ ); their magmatic ages are therefore considered reliable. The age of the youngest detrital zircons in the tuffaceous slate sample is  $353.6 \pm 5.1$  Ma, which constrains the time of deposition as not older than early Carboniferous. A significant feature of the sample is that it has unimodal detrital zircon style with peak ages of 356 Ma, close to their youngest detrital zircon age; the youngest age suggests that early Palaeozoic oceanic subduction in the Central Beishan accretionary collage was ongoing until early

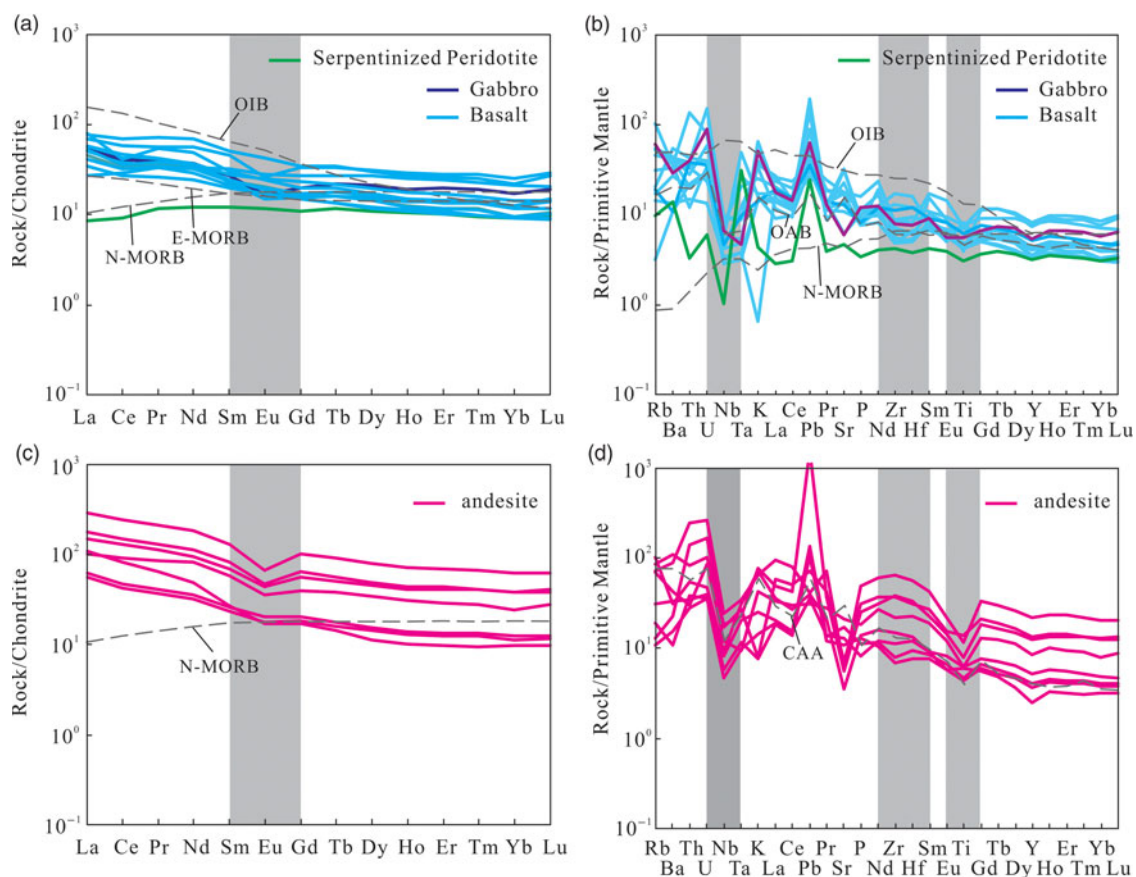


**Fig. 7.** (a, b) Chondrite-normalized rare earth element patterns and primitive mantle-normalized spider diagram for basalts, gabbro and serpentinized peridotite from the Mazongshan complex. (c, d) Chondrite-normalized REE patterns and primitive mantle-normalized spider diagram for andesite; standardization values are from Sun & McDonough (1989). CAA – continental-arc andesite; OAB – oceanic-arc basalt; MORB – mid-ocean-ridge basalt.

Carboniferous time. These new data are inconsistent with previous theories that the early Palaeozoic Palaeo-Asian Ocean closed during the Devonian Period.

Most accretionary orogenic belts worldwide undergo complex tectonic processes, such as subduction, accretion and collision (Windley, 1992; Isozaki, 1996; Cawood *et al.* 2009; Xiao *et al.* 2010; Wakabayashi, 2011; Safonova & Santosh, 2014). It is particularly difficult to unravel the differential ages of the tectonic fragments in mélanges, regardless of whether they formed in oceanic-island arcs, continental-margin arcs or fore-arc basins. The Beishan subduction–accretion collage occupies a key position within the CAOB and contains the Mazongshan complex, which contains critical data that can help to constrain the evolution of the central Beishan collage, particularly of the complicated HNMX ophiolitic mélange.

The Mazongshan complex is situated in the southern Gongpoquan arc, and is close to the HNMX ophiolitic mélange. Using new geological maps and geochemical data, Song *et al.* (2013a, b, 2014, 2015) recently suggested that the Lebaquan arc–fore-arc complex belongs to the Gongpoquan arc rather than the Mazongshan complex settings. Notably, Kazakhstan and North Tien Shan are composed of several arc–basin systems, which show a complicated tectonic massif during early Palaeozoic time (Degtyarev, 2011; Safonova *et al.* 2019). Some recently acquired data suggest that accretion events did not cease during the Silurian Period (Shu *et al.* 2007). We propose that the accretion events to

the north of the HNMX ophiolitic mélange are similar to the eastern segment of Kazakhstan in terms of structure, geochronology and subduction polarity.

## 6.b. Petrogenesis and tectonic setting of the Mazongshan complex

### 6.b.1. Gabbro and basalts

The gabbro and basalts from the Mazongshan mélange have similar geochemical compositions (Fig. 7; Table 1) in that they all have slightly enriched REE patterns on chondrite-normalized diagrams. However, on normal- (N-) MORB-normalized diagrams, the gabbro and basalts have different high-field-strength element (HFSE) trace-element patterns (Fig. 7b).

It is well known that the geochemical signatures of island-arc basalts are indicated by high LILE/HFSE and LREE/HREE ratios and low Nb/U and Ce/Pb ratios. In contrast, N-MORB-like geochemical signatures are indicated by low LILE/HFSE and LREE/HREE ratios. As a result of hydrothermal alteration by seawater, igneous oceanic crust acquires variably elevated abundances of LILE and Pb relative to N-MORB, so seafloor sediments show significant enrichments in LILE, Pb, LREE, Nb and Ta compared with MORB, despite the Nb–Ta trough in the diagram (Fig. 7b; Zheng, 2019). The gabbro and basalts exhibit variable contents of Zr (54.91–194.30 ppm), Nb (2.04–6.85 ppm), Ta (0.13–2.03 ppm) and Hf (1.58–4.93 ppm), which are close to those of typical modern

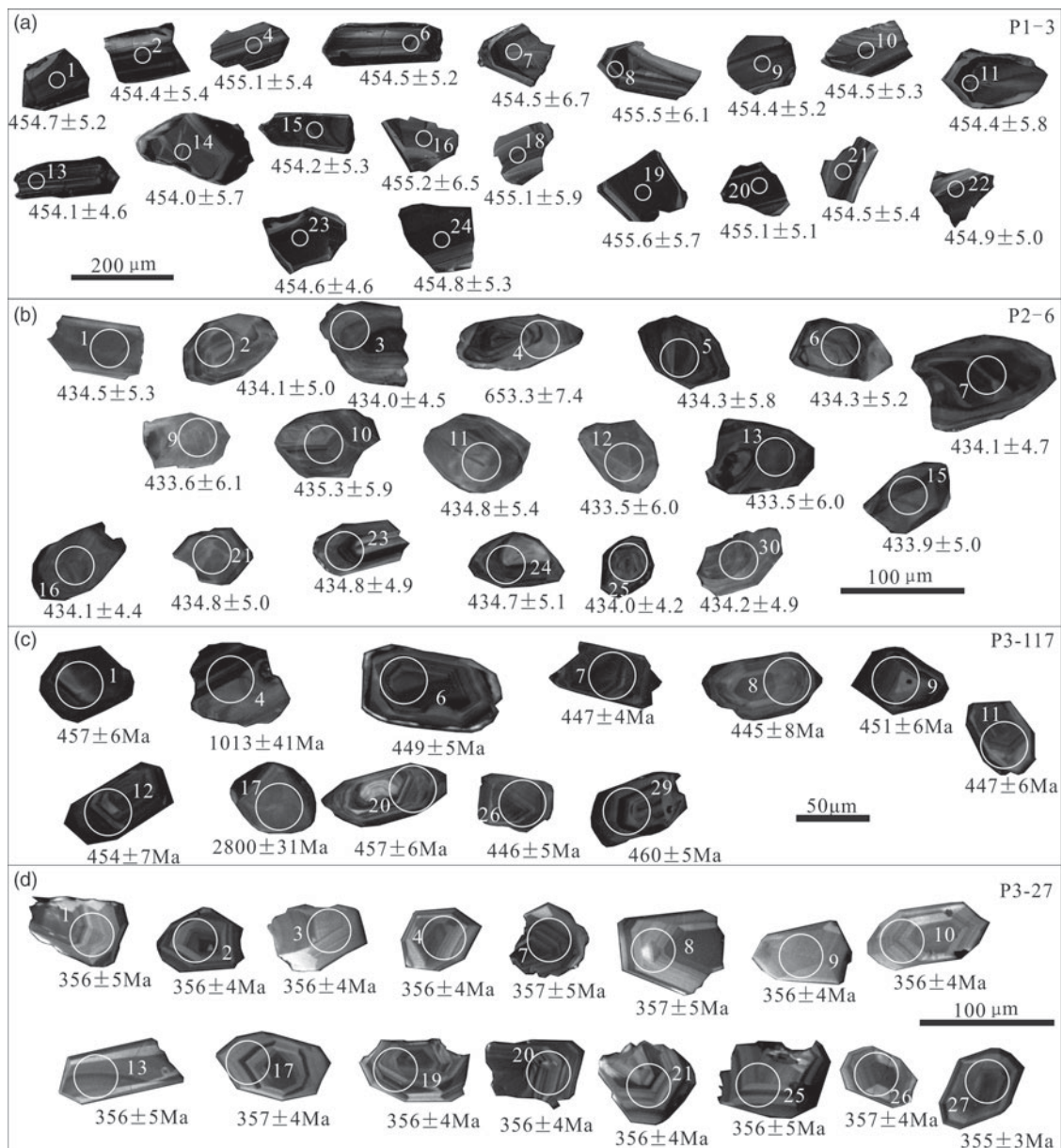


**Fig. 8.** Cathodoluminescence images and U–Pb ages of zircons from the Mazongshan complex: (a) cumulate gabbro sample P1-3; (b) gabbro sample P2-6; (c) andesite sample P3-117; (d) tuffaceous slate sample P3-27.

oceanic arcs (Sun & McDonough, 1989; Stolz *et al.* 1996; Flidner & Klemperer, 2000). The Zr/Nb ratios of the gabbro and basalts range from 9.52 to 64.56, which is close to the range of MORB. On chondrite-normalized diagrams (Fig. 7a), the Mazongshan gabbro and group 1 basalts are similar to those of enriched (E-) MORB. Moreover, on primitive mantle-normalized diagrams (Fig. 7b), the geochemical characteristics of the gabbro and group 1 basalts range from altered oceanic basalts to oceanic-arc basalts (OAB). The difference in HFSEs suggests that the sedimentary input to the subduction zone was highly variable. Continental margins adjacent to oceanic subduction zones generally undergo chemical weathering during subduction, transporting a variety of material into the trench including water-soluble elements and water-insoluble detritus.

On the V–Ti/1000 diagram (Fig. 11c), the gabbro and group 1 basalts have low V contents and moderate Ti/V ratios, mainly

located in the MORB field. In the Th–Hf/3–Ta discrimination diagram (Fig. 11a), most of our basalts plot in the field of subduction-related, calc-alkaline basalts. This may suggest derivation in an active continental margin, suggesting that the MORB-like source material had been overprinted by subduction-derived components before the partial melting. This conclusion is further supported by the higher Th contents and Th/Yb ratios than those typical of MORB. In general, the metasomatizing agents in subduction zones are mainly hydrous melts and slab-derived fluids (Brenan *et al.* 1995; Elliott *et al.* 1997; Castillo *et al.* 2002; Zheng, 2012). Accordingly, these relevant chemical distinctions indicate that the gabbro and group 1 basalts most likely formed as juvenile oceanic rocks in a supra-subduction zone setting (Davies & Stevenson, 1992; Stolz *et al.* 1996; Davidson & Arculus, 2006; Kröner *et al.* 2008; Dilek & Furnes, 2011, 2014).

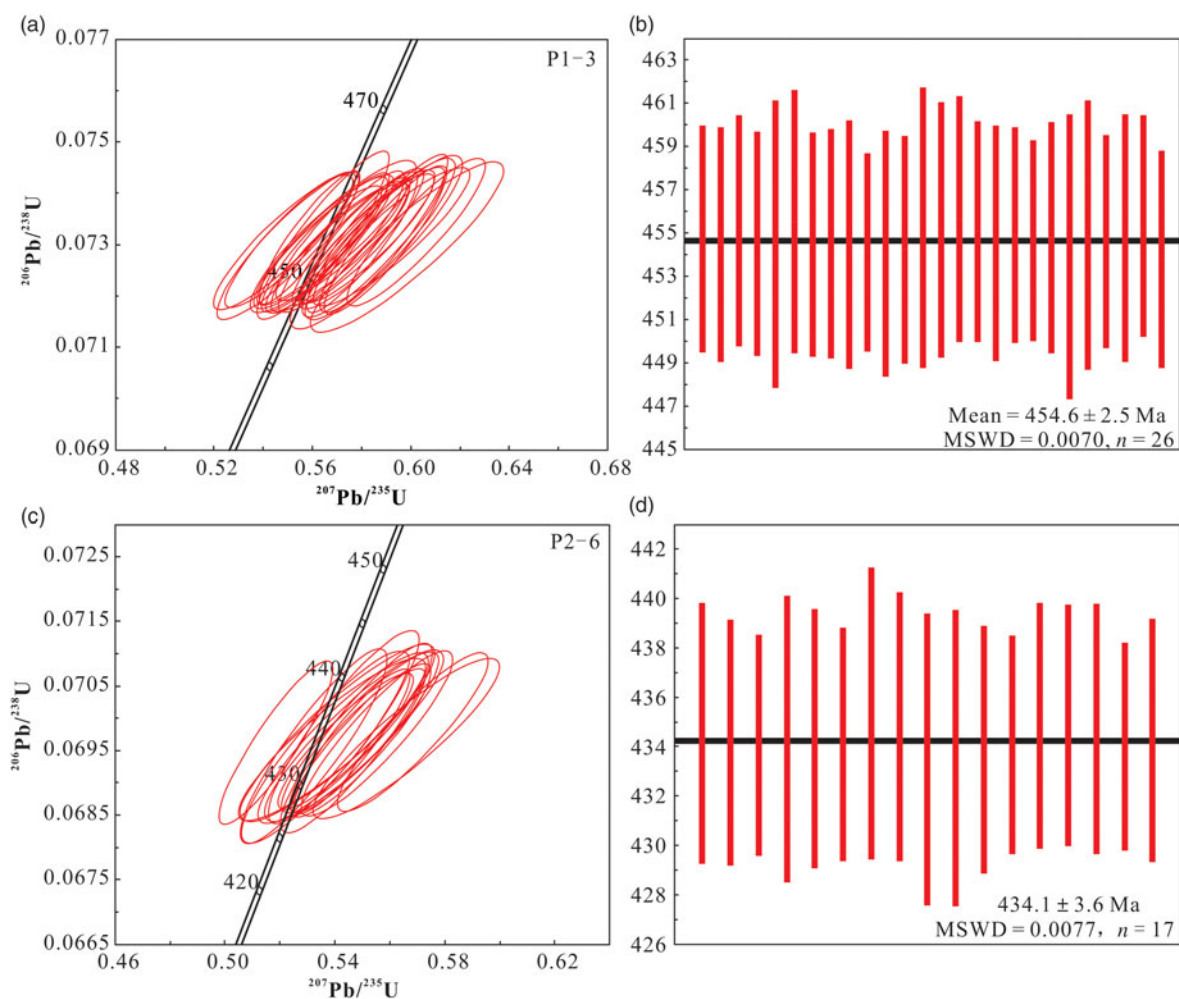


**Fig. 9.** (Colour online) The Mazongshan complex. (a) U–Pb concordia diagrams for zircons from cumulate gabbro sample P1-3; (b) weighted average  $^{206}\text{Pb}/^{238}\text{U}$  ages from cumulate gabbro sample P1-3; (c) U–Pb concordia diagrams for zircons from gabbro sample P2-6; and (d) weighted average  $^{206}\text{Pb}/^{238}\text{U}$  ages from gabbro sample P2-6.

### 6.b.2. Andesites

The andesites are characterized by enrichments of LREE and variable enrichments of HREE (Fig. 7b, d). On Th/Yb v. Ta/Yb diagrams (Fig. 11b), the andesites plot in the active continental-arc field, but the  $\text{TiO}_2$  content is higher than that of continental arcs. Collectively, the geochemical signatures indicate that the andesites formed in an oceanic-arc setting (Sun & McDonough, 1989; Stolz *et al.* 1996; Fließner & Klemperer, 2000).

The blocks in the Mazongshan ophiolitic mélange underwent extensive deformation and metamorphism during accretion and emplacement, resulting in fragmentation, shearing and intrusion of hydrothermal veins. Both basalts and andesites exhibit obvious depletions in Nb–Ta, suggesting that their magmas were generated in modern subduction zone settings and that they were affected by continental contamination (Davidson & Arculus, 2006). However, the plots of MgO v. Zr, Th and Nb/La show no correlations, suggesting that crustal contamination played an insignificant role in their genesis (Fig. 12).

### 6.b.3. Tectonic setting

We used initial field characteristics to distinguish between the basalts and andesites. However, they both formed during a similar age range (Fig. 2). Our geochemical study reveals that the basic–intermediate rocks in the mélanges consist of subduction-modified

E-MORB-like rocks that likely formed in a back-arc basin and arc-related andesites.

The process of accretion incorporates the concept of ocean–continent transition as follows: oceanic crust grows at a mid-oceanic ridge from a plume generated in the mantle transition zone at a depth of c. 440–660 km. An immature arc grows in an ocean by subduction; considering that such arcs can reach some 50 km in thickness, their formation in a supra-subduction zone setting is not far below that depth. Mature continental crust grows at an active continental margin that starts from partial melting of a shallow-dipping oceanic slab as in the Andes, and progresses via emplacement of the magma through the continental crust. An ocean–continent transition is therefore an important tectonic zone within the plate tectonic paradigm, because it records the change from a deep mantle oceanic source to a shallower continental or shallow mantle condition. The co-existence of MORB and IAT rocks has rarely been documented in the Mazongshan complex, where an immature arc crust has grown into a mature arc-continental crust, as in the Coast Range complex of California (e.g. Shervais, 2001; Reagan *et al.* 2010; Xiao *et al.* 2016). Considering the lithological, structural, geochronological and geochemical characteristics of the Mazongshan complex, we propose that it formed in a single back-arc basin that formed above a NW-dipping intra-oceanic subduction zone during Late Ordovician to

**Table 2.** U–Pb data for the zircons from samples of the Mazongshan complex

Spot no.	Th (ppm)	U (ppm)	Th/U	Isotopic ratio				Age (Ma)			
				$^{207}\text{Pb}/^{235}\text{U}$	1 $\sigma$	$^{206}\text{Pb}/^{238}\text{U}$	1 $\sigma$	$^{207}\text{Pb}/^{235}\text{U}$	1 $\sigma$	$^{206}\text{Pb}/^{238}\text{U}$	1 $\sigma$
Lithology, P1-3 gabbro											
P1-3-01	219.41	441.23	0.50	0.5511	0.0174	0.0731	0.0009	445.7	11.4	454.7	5.3
P1-3-02	730.30	771.69	0.95	0.5801	0.0148	0.0730	0.0009	464.5	9.5	454.5	5.4
P1-3-04	141.35	300.91	0.47	0.5921	0.0210	0.0732	0.0009	472.2	13.4	455.1	5.4
P1-3-06	299.47	490.71	0.61	0.5646	0.0187	0.0730	0.0009	454.5	12.2	454.5	5.2
P1-3-07	129.21	279.95	0.46	0.5860	0.0231	0.0730	0.0011	468.3	14.8	454.5	6.7
P1-3-08	528.91	693.03	0.76	0.5889	0.0172	0.0732	0.0010	470.2	11.0	455.5	6.1
P1-3-09	171.01	348.90	0.49	0.5482	0.0186	0.0730	0.0009	443.8	12.2	454.5	5.2
P1-3-10	370.12	535.38	0.69	0.5670	0.0159	0.0731	0.0009	456.1	10.3	454.5	5.3
P1-3-11	208.28	414.36	0.50	0.5848	0.0191	0.0730	0.0010	467.5	12.3	454.5	5.8
P1-3-13	436.65	603.35	0.72	0.5626	0.0168	0.0730	0.0008	453.2	10.9	454.1	4.6
P1-3-14	210.87	393.19	0.54	0.5500	0.0190	0.0730	0.0009	445.0	12.5	454.0	5.7
P1-3-15	489.73	593.23	0.83	0.5649	0.0168	0.0730	0.0009	454.7	10.9	454.2	5.3
P1-3-16	129.67	295.88	0.44	0.5645	0.0178	0.0732	0.0011	454.5	11.6	455.3	6.5
P1-3-18	162.06	352.85	0.46	0.5684	0.0222	0.0732	0.0010	457.0	14.4	455.1	5.9
P1-3-19	530.93	683.92	0.78	0.6021	0.0184	0.0732	0.0009	478.6	11.7	455.6	5.7
P1-3-20	1378.59	1148.79	1.20	0.5587	0.0135	0.0731	0.0009	450.7	8.8	455.1	5.1
P1-3-21	353.56	508.50	0.70	0.5718	0.0169	0.0731	0.0009	459.2	10.9	454.5	5.5
P1-3-22	345.59	480.74	0.72	0.5822	0.0180	0.0731	0.0008	465.9	11.5	454.9	5.0
P1-3-23	424.58	666.90	0.64	0.5717	0.0175	0.0731	0.0008	459.1	11.3	454.6	4.7
P1-3-24	603.67	719.69	0.84	0.5820	0.0182	0.0731	0.0009	465.8	11.7	454.8	5.4
P1-3-25	124.83	268.79	0.46	0.5984	0.0259	0.0729	0.0011	476.2	16.5	453.9	6.6
P1-3-26	357.48	558.50	0.64	0.5874	0.0202	0.0731	0.0010	469.2	12.9	454.9	6.2
P1-3-27	661.85	785.31	0.84	0.5757	0.0158	0.0731	0.0008	461.7	10.2	454.6	4.9
P1-3-28	762.45	842.94	0.90	0.5898	0.0164	0.0731	0.0010	470.7	10.5	454.8	5.7
P1-3-29	356.57	490.37	0.73	0.5801	0.0167	0.0732	0.0009	464.5	10.7	455.3	5.1
P1-3-30	240.81	426.59	0.56	0.5703	0.0192	0.0729	0.0008	458.2	12.4	453.8	5.0
Lithology, P2-6 gabbro											
P2-6-01	158.13	202.57	0.78	0.5469	0.0215	0.0697	0.0009	443.0	14.1	434.5	5.3
P2-6-02	141.77	194.63	0.73	0.5390	0.0224	0.0697	0.0008	437.8	14.8	434.1	5.0
P2-6-03	114.98	524.13	0.22	0.5462	0.0139	0.0696	0.0007	442.5	9.1	434.0	4.5
P2-6-04	142.99	320.70	0.45	0.9398	0.0240	0.1067	0.0013	672.8	12.6	653.3	7.4
P2-6-05	160.09	498.23	0.32	0.5479	0.0182	0.0697	0.0010	443.7	11.9	434.3	5.8
P2-6-06	95.97	242.60	0.40	0.5430	0.0205	0.0697	0.0009	440.4	13.5	434.3	5.2
P2-6-07	1470.44	608.64	2.42	0.5495	0.0169	0.0697	0.0008	444.7	11.1	434.1	4.7
P2-6-09	77.88	113.49	0.69	0.5743	0.0272	0.0696	0.0010	460.8	17.5	433.6	6.1
P2-6-10	185.55	196.08	0.95	0.5432	0.0180	0.0699	0.0010	440.5	11.9	435.3	5.9
P2-6-11	106.97	166.33	0.64	0.5410	0.0234	0.0698	0.0009	439.1	15.4	434.8	5.4
P2-6-12	98.80	180.94	0.55	0.5364	0.0201	0.0696	0.0010	436.0	13.3	433.5	5.9
P2-6-13	161.33	266.35	0.61	0.5323	0.0177	0.0696	0.0010	433.4	11.7	433.5	6.0
P2-6-15	84.10	350.48	0.24	0.5185	0.0137	0.0696	0.0008	424.2	9.2	433.9	5.0
P2-6-16	117.40	328.56	0.36	0.5482	0.0164	0.0697	0.0007	443.8	10.7	434.1	4.4

(Continued)

Table 2. (Continued)

Spot no.	Th (ppm)	U (ppm)	Th/U	Isotopic ratio				Age (Ma)			
				$^{207}\text{Pb}/^{235}\text{U}$	1 $\sigma$	$^{206}\text{Pb}/^{238}\text{U}$	1 $\sigma$	$^{207}\text{Pb}/^{235}\text{U}$	1 $\sigma$	$^{206}\text{Pb}/^{238}\text{U}$	1 $\sigma$
P2-6-21	123.05	227.30	0.54	0.5491	0.0188	0.0698	0.0008	444.4	12.3	434.8	5.0
P2-6-23	171.52	402.59	0.43	0.5683	0.0180	0.0698	0.0008	456.9	11.7	434.9	4.9
P2-6-24	131.41	285.75	0.46	0.5554	0.0181	0.0698	0.0008	448.5	11.8	434.7	5.1
P2-6-25	312.26	439.49	0.71	0.5439	0.0164	0.0696	0.0007	441.0	10.8	434.0	4.2
P2-6-30	101.98	183.21	0.56	0.5660	0.0223	0.0697	0.0008	455.4	14.5	434.2	4.9
Lithology, P3-117 andesite											
P3-117-01	104.25	271.01	0.38	0.5687	0.0219	0.0735	0.0010	457.2	14.1	457.0	5.7
P3-117-06	133.48	233.96	0.57	0.5667	0.0223	0.0721	0.0008	455.9	14.4	448.8	5.1
P3-117-07	372.91	691.46	0.54	0.5407	0.0158	0.0718	0.0007	438.9	10.4	446.7	4.4
P3-117-08	126.56	131.57	0.96	0.5682	0.0279	0.0715	0.0014	456.8	18.1	445.5	8.3
P3-117-09	149.61	197.03	0.76	0.5267	0.0303	0.0725	0.0010	429.6	20.1	451.5	6.3
P3-117-11	178.18	275.91	0.65	0.5352	0.0199	0.0717	0.0009	435.3	13.2	446.7	5.5
P3-117-12	201.05	409.23	0.49	0.5682	0.0195	0.0730	0.0011	456.9	12.6	454.0	6.5
P3-117-20	86.35	279.14	0.31	0.5346	0.0188	0.0735	0.0010	434.9	12.4	457.0	6.0
P3-117-26	178.33	307.08	0.58	0.5616	0.0287	0.0717	0.0009	452.6	18.7	446.4	5.4
P3-117-29	287.83	480.09	0.60	0.5695	0.0162	0.0739	0.0008	457.7	10.5	459.9	5.0
P3-117-04	270.74	523.77	0.52	1.7130	0.0370	0.1694	0.0019	1013.4	13.9	1008.9	10.6
P3-117-17	129.35	222.96	0.58	9.3136	0.1795	0.4340	0.0039	2369.4	17.7	2323.8	17.5
Lithology, P3-27 tuffaceous slate											
P3-27-01	73.32	175.36	0.42	0.5687	0.0219	0.0735	0.0010	366.1	13.5	356.0	4.6
P3-27-02	244.22	359.26	0.68	0.5667	0.0223	0.0721	0.0008	352.2	10.4	356.4	3.6
P3-27-03	61.87	159.61	0.39	0.5407	0.0158	0.0718	0.0007	375.4	12.6	356.3	4.4
P3-27-04	169.01	304.69	0.55	0.5682	0.0279	0.0715	0.0014	363.1	9.3	356.4	3.7
P3-27-07	190.75	324.27	0.59	0.5267	0.0303	0.0725	0.0010	370.8	10.8	356.9	4.6
P3-27-08	86.34	195.83	0.44	0.5352	0.0199	0.0717	0.0009	372.4	11.3	356.6	4.5
P3-27-09	71.76	163.74	0.44	0.4530	0.0183	0.0568	0.0007	379.3	12.8	356.3	4.2
P3-27-10	72.20	173.06	0.42	0.4186	0.0195	0.0568	0.0007	355.0	14.0	356.4	4.2
P3-27-13	77.92	161.48	0.48	0.4524	0.0191	0.0568	0.0008	379.0	13.4	356.4	5.0
P3-27-17	118.11	256.66	0.46	0.3995	0.0139	0.0569	0.0006	341.3	10.1	356.5	3.9
P3-27-19	180.04	289.82	0.62	0.4396	0.0158	0.0567	0.0007	370.0	11.2	355.8	4.2
P3-27-20	168.99	273.02	0.62	0.4684	0.0166	0.0568	0.0007	390.1	11.5	356.3	4.0
P3-27-21	182.80	290.57	0.63	0.4194	0.0136	0.0567	0.0006	355.6	9.7	355.8	3.7
P3-27-25	132.73	244.35	0.54	0.4218	0.0176	0.0568	0.0007	357.3	12.6	356.1	4.6
P3-27-26	171.35	318.94	0.54	0.4539	0.0159	0.0569	0.0007	380.0	11.1	356.5	4.3
P3-27-27	311.27	428.92	0.73	0.4339	0.0124	0.0566	0.0006	365.9	8.8	355.1	3.4
P3-27-28	110.80	231.51	0.48	0.4342	0.0165	0.0569	0.0007	366.2	11.7	356.5	4.4
P3-27-29	106.31	217.59	0.49	0.4534	0.0162	0.0568	0.0007	379.7	11.3	356.4	4.5
P3-27-31	79.10	164.89	0.48	0.4261	0.0182	0.0569	0.0012	360.4	13.0	356.8	7.6
P3-27-33	102.41	226.08	0.45	0.4526	0.0181	0.0568	0.0008	379.1	12.7	356.1	4.6
P3-27-34	162.05	283.08	0.57	0.4307	0.0149	0.0567	0.0007	363.7	10.6	355.6	4.1
P3-27-37	96.29	185.06	0.52	0.4530	0.0221	0.0568	0.0007	379.4	15.4	355.9	4.4
P3-27-38	83.23	218.90	0.38	0.4678	0.0183	0.0569	0.0008	389.6	12.6	356.5	4.9

(Continued)

**Table 2.** (Continued)

Spot no.	Th (ppm)	U (ppm)	Th/U	Isotopic ratio				Age (Ma)			
				<sup>207</sup> Pb/ <sup>235</sup> U	1σ	<sup>206</sup> Pb/ <sup>238</sup> U	1σ	<sup>207</sup> Pb/ <sup>235</sup> U	1σ	<sup>206</sup> Pb/ <sup>238</sup> U	1σ
P3-27-41	344.68	455.02	0.76	0.4354	0.0138	0.0567	0.0007	367.0	9.7	355.3	4.1
P3-27-43	133.68	256.99	0.52	0.3838	0.0213	0.0564	0.0008	329.8	15.6	353.6	5.1
P3-27-46	485.62	576.66	0.84	0.4537	0.0130	0.0567	0.0006	379.9	9.1	355.7	3.5
P3-27-47	153.59	302.22	0.51	0.4459	0.0155	0.0569	0.0008	374.4	10.9	356.8	4.7
P3-27-49	119.92	244.30	0.49	0.4669	0.0191	0.0569	0.0007	389.1	13.2	356.5	4.4
P3-27-53	162.58	282.20	0.58	0.4235	0.0150	0.0569	0.0007	358.5	10.7	356.7	4.4
P3-27-54	90.94	202.78	0.45	0.4390	0.0180	0.0568	0.0007	369.6	12.7	356.1	4.0
P3-27-55	55.54	151.59	0.37	0.4234	0.0212	0.0567	0.0008	358.5	15.1	355.7	5.0
P3-27-56	117.21	183.64	0.64	0.4328	0.0171	0.0567	0.0007	365.2	12.1	355.5	4.5
P3-27-58	200.05	339.10	0.59	0.4441	0.0163	0.0568	0.0007	373.2	11.5	355.9	4.4
P3-27-61	52.15	141.09	0.37	0.4489	0.0270	0.0567	0.0008	376.5	18.9	355.6	4.9
P3-27-62	46.40	138.94	0.33	0.4203	0.0227	0.0568	0.0007	356.3	16.2	356.3	4.5
P3-27-63	188.01	311.93	0.60	0.4543	0.0163	0.0570	0.0009	380.3	11.4	357.1	5.2
P3-27-64	375.52	485.88	0.77	0.4241	0.0135	0.0569	0.0006	359.0	9.6	356.5	3.9
P3-27-67	38.03	111.20	0.34	0.4612	0.0243	0.0567	0.0009	385.1	16.9	355.6	5.5
P3-27-68	55.57	147.57	0.38	0.4134	0.0194	0.0568	0.0008	351.3	14.0	356.2	4.8
P3-27-69	216.79	363.83	0.60	0.4460	0.0143	0.0568	0.0007	374.5	10.0	356.4	4.0
P3-27-73	144.63	235.78	0.61	0.4436	0.0185	0.0569	0.0008	372.8	13.0	356.6	4.6
P3-27-74	128.95	247.93	0.52	0.4372	0.0162	0.0568	0.0007	368.3	11.5	356.3	4.5
P3-27-78	259.18	367.71	0.70	0.4774	0.0153	0.0574	0.0007	396.3	10.5	360.0	4.2
P3-27-80	83.13	192.18	0.43	0.4182	0.0169	0.0568	0.0007	354.8	12.1	356.3	4.3
P3-27-82	89.29	216.00	0.41	0.4481	0.0159	0.0568	0.0007	375.9	11.2	356.3	4.5
P3-27-83	80.68	191.62	0.42	0.4286	0.0250	0.0570	0.0008	362.2	17.8	357.2	4.6
P3-27-85	243.93	378.99	0.64	0.4260	0.0172	0.0576	0.0007	360.4	12.3	360.9	4.5
P3-27-86	370.12	443.02	0.84	0.4712	0.0313	0.0575	0.0008	392.0	21.6	360.7	5.0
P3-27-87	217.39	321.75	0.68	0.4976	0.0194	0.0598	0.0008	410.1	13.1	374.4	4.6
P3-27-88	115.00	242.60	0.47	0.4211	0.0182	0.0569	0.0008	356.9	13.0	356.9	5.0
P3-27-90	110.15	209.41	0.53	0.4285	0.0173	0.0567	0.0007	362.1	12.3	355.7	4.3
P3-27-91	147.26	294.69	0.50	0.4364	0.0161	0.0569	0.0008	367.7	11.4	356.9	5.0
P3-27-95	173.74	299.22	0.58	0.4315	0.0150	0.0568	0.0008	364.2	10.6	355.9	4.8
P3-27-96	126.35	233.86	0.54	0.4013	0.0145	0.0568	0.0007	342.6	10.5	356.1	4.2
P3-27-95	173.74	299.22	0.58	0.4315	0.0150	0.0568	0.0008	364.2	10.6	355.9	4.8

earliest middle Silurian time (Fig. 13b). As subduction continued, these rocks evolved into the HNMX ophiolitic mélange until the Carboniferous Period.

### 6.c. Implications and tectonic evolution

The evolution of the Mazongshan subduction–accretion complex took place over the following four stages (Fig. 13).

(1) An ocean opened along an accreting tectonic boundary of the HNMX ophiolitic mélange during early Cambrian time, as revealed by high-resolution geochronology and field characteristics (Gangu Survey Institute, 2001; Chen *et al.* 2017; Shi *et al.* 2018).

(2) During a second stage, the passive continental margin was transformed into an active continental margin. The EW-trending Gongpoquan arc developed on the southern margin of the Mingshui–Hanshan Massif, and the HNMX ophiolitic mélange, which is made of MORB-type basalts and gabbros, formed during N-wards oceanic subduction beneath the Mingshui–Hanshan Massif (Ao *et al.* 2012; Song *et al.* 2015; Wang *et al.* 2017). The emplacement of the northern Lebaquan complex, the product of N-dipping subduction and other events within the Mazongshan complex during Ordovician – late Silurian time (Song *et al.* 2015), suggests that intra-ocean subduction continued until at least Middle Ordovician time (Ao *et al.* 2012).



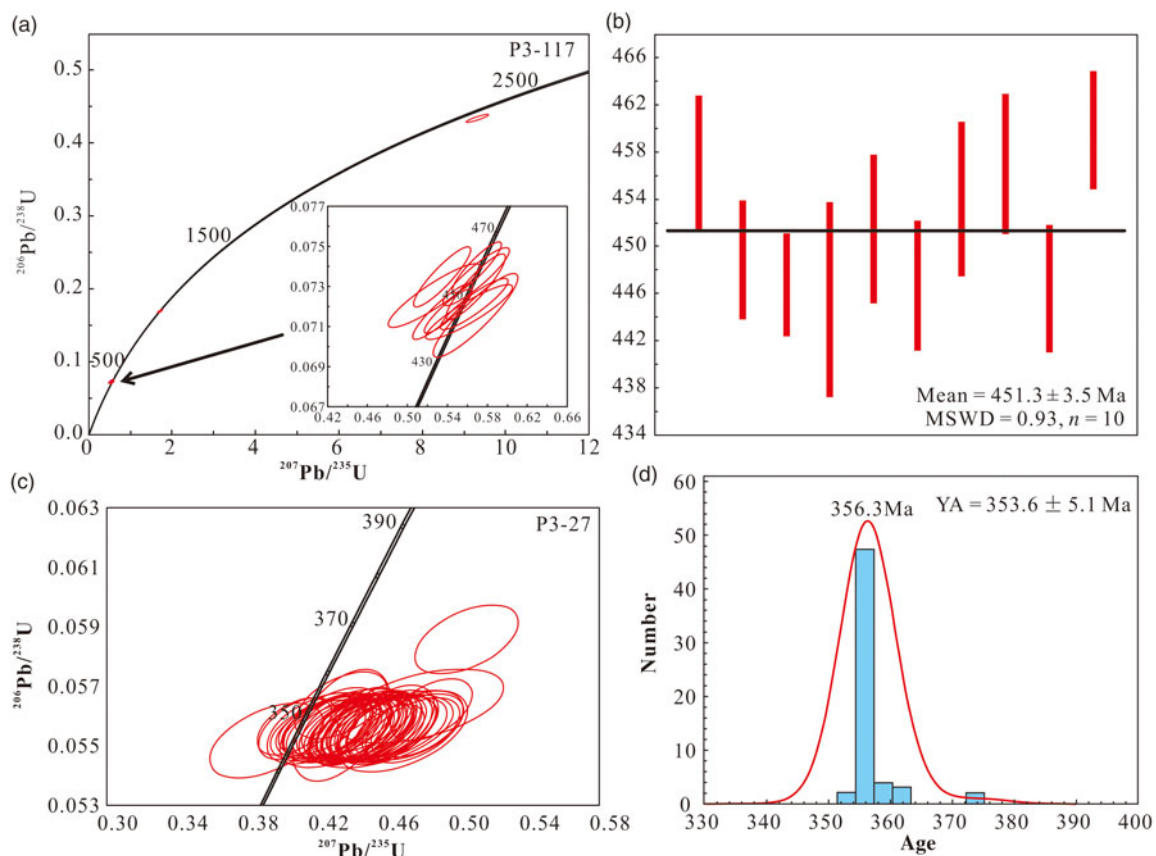


**Fig. 10.** (Colour online) The Mazongshan complex. (a) U-Pb concordia diagrams for zircons from andesite sample P3-117; (b) weighted average  $^{206}\text{Pb}/^{238}\text{U}$  ages from andesite sample P3-117; (c) U-Pb concordia diagrams for zircons from tuffaceous slate sample P3-27; and (d) probability histograms  $^{206}\text{Pb}/^{238}\text{U}$  ages from tuffaceous slate sample P3-27, Y.A.-the youngest age.

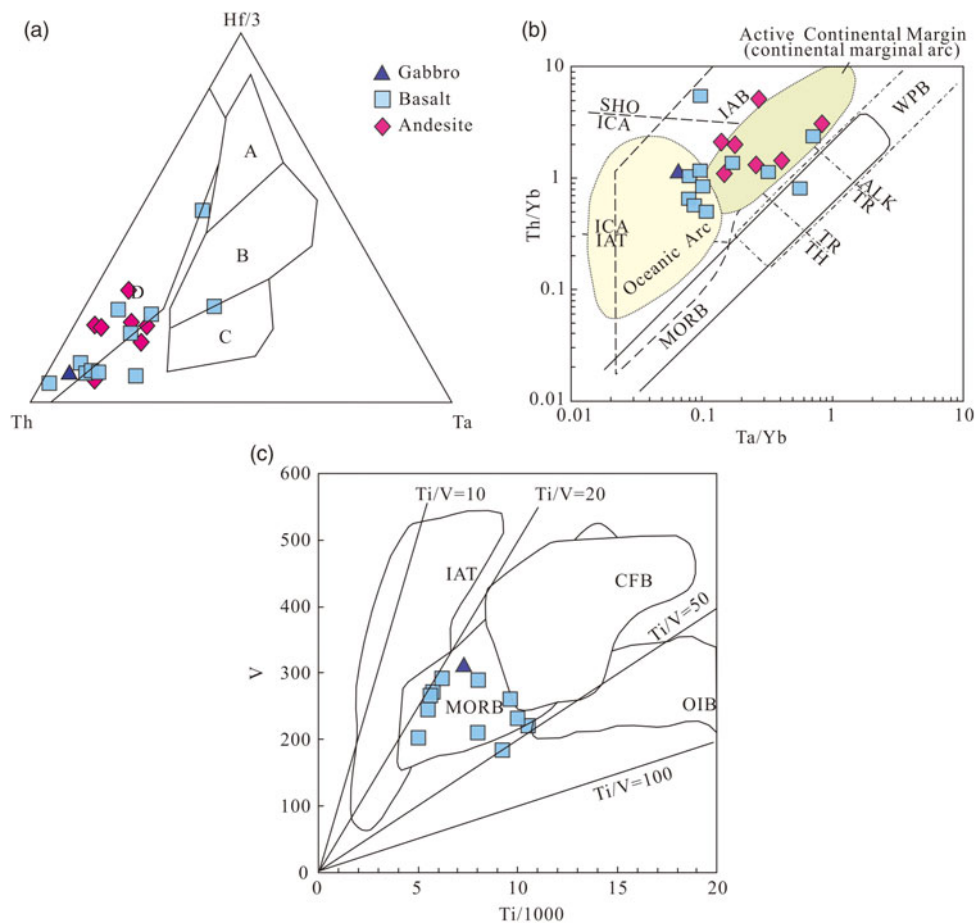


**Fig. 11.** (Colour online) Tectonic discrimination diagrams for the gabbro, basalts and andesites of the Mazongshan complex. (a) Th-Hf/3-Ta discrimination diagram (after Wood, 1980); A, N-MORB; B, E-MORB; C, OIB; D, calc-alkaline. (b) Th/Yb v. Ta/Yb diagram (after Pearce, 2008, 2014); (c) V v. Ti/1000 diagram (after Shervais, 1982). Triangles, gabbro; squares, basalt; diamonds, andesite.

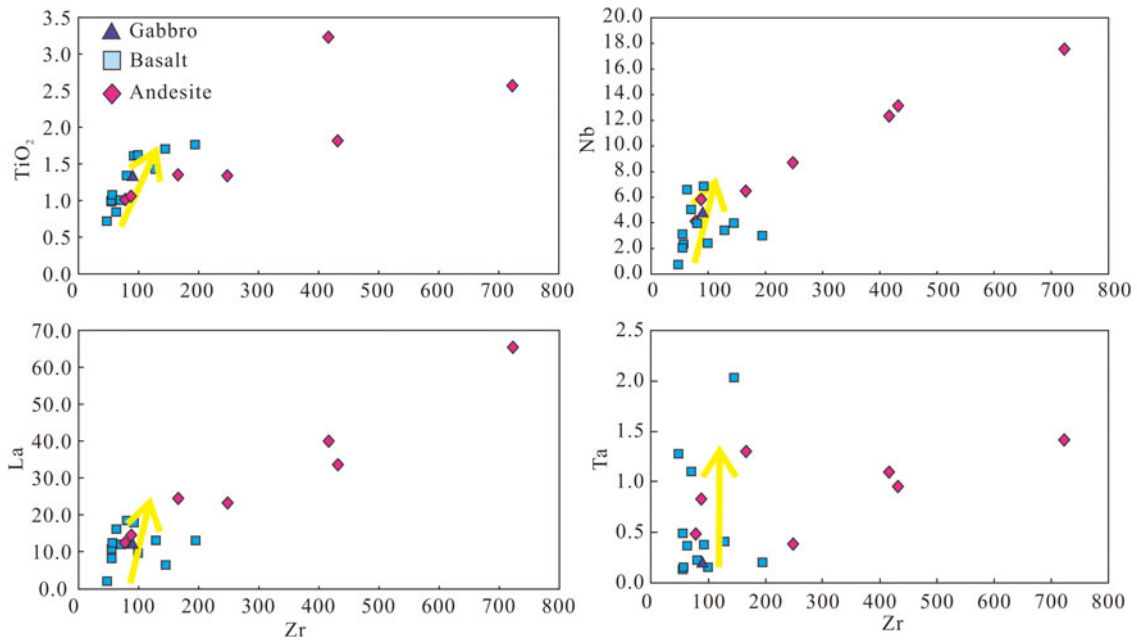


**Fig. 12.** Plots of Zr v.  $\text{TiO}_2$ , La, Nb and Ta for the gabbro, basalts and andesites of the Mazongshan complex. Triangles, gabbro; squares, basalt; diamonds, andesite.

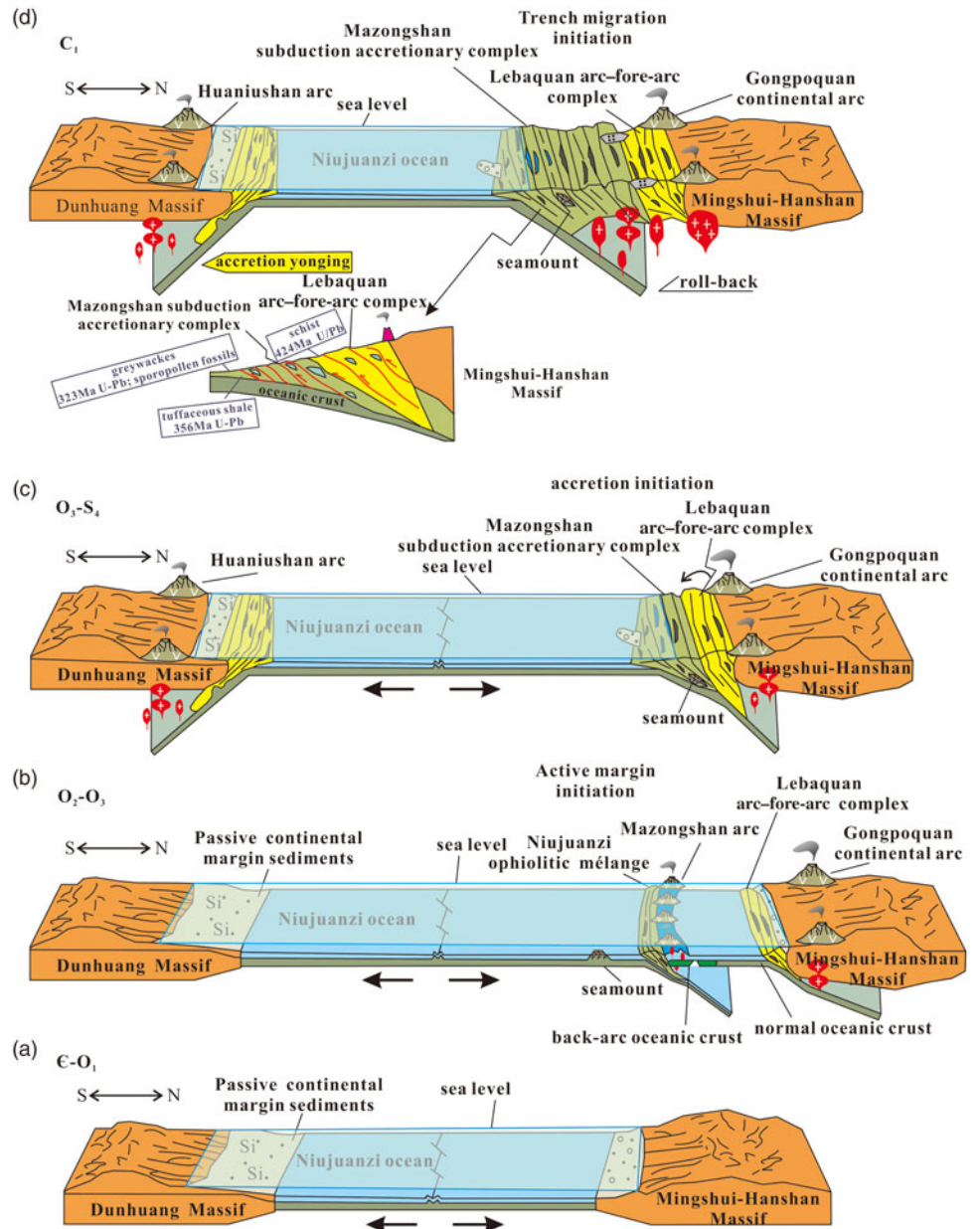


**Fig. 13.** Tectonic evolution of the central Beishan accretionary collage, emphasizing the sequential spatial relationships of the Mazongshan complex (modified by Ao *et al.* 2012; Wang *et al.* 2017). (a) Cambrian – Early Ordovician: the Niujuanzi Ocean was expanding, as indicated by Sinian moraine gravels situated in the two flanks of the HNMX ophiolitic mélangé; age of ophiolites by Hou *et al.* (2012), Tian *et al.* (2014) and Shi *et al.* (2018). (b) Middle–Late Ordovician: Niujuanzi oceanic crust subducted N-wards beneath the Mingshui–Hanshan massif at least since Middle Ordovician time, forming the Mazongshan intra-arc-basin system during Late Ordovician time (after Ao *et al.* 2012; Song *et al.* 2015). (c) Late Ordovician – late Silurian: magmatic activity peaked on both sides of the HNMX, which suggests bidirectional subduction and shrinkage of the Niujuanzi Ocean (Mao *et al.* 2012; Zheng *et al.* 2018, 2019). (d) Early Devonian – early Carboniferous: the youngest age of the turbidites indicates that accretionary growth continued to the north until early Carboniferous time (Wang *et al.* 2018a).

- (3) Magmatic activity peaked during Late Ordovician – late Silurian time (Zuo *et al.* 1994; Xiao *et al.* 2010; Mao *et al.* 2012; Song *et al.* 2014; Ding *et al.* 2015; Wang *et al.* 2018b; Zheng *et al.* 2019). With continuous N-wards subduction of the Palaeo-Asian Ocean, andesites and basalt–andesite–rhyolite–quartz–trachyte–trachy basalts were extruded in the Gongpoquan subduction-generated arc (Wang *et al.* 2016, 2018b; Zheng *et al.* 2019). Our chemical and age data suggest that the Mazongshan complex formed in a back-arc basin that began to shrink as a result of the N-wards subduction of the Niujuanzi Ocean or Palaeo-Asian Ocean during Late Ordovician – early Carboniferous time. By considering the timing (Xiao *et al.* 2010; Mao *et al.* 2012; Ding *et al.* 2015), we can conclude that the southern magmatic arc in the central Beishan accretionary collage resulted from two-way subduction of the Niujuanzi Ocean after Late Ordovician Epoch.
- (4) The final stage of evolution was the migration of the Mazongshan subduction–accretion complex towards the ocean during late Silurian – Carboniferous time. During early Silurian – Early Devonian time, the Niujuanzi Ocean may have been subducting beneath the accretionary wedge. During this process, extensive Silurian–Devonian magmatism resulted from the subduction of a spreading ridge and the opening of a slab window (Zheng *et al.* 2018, 2019). The central Beishan accretionary collage is a complicated region, in which subduction apparently began from the Late Ordovician Epoch (454.6 Ma). Integration with other published data suggests that the younging direction of accretion was from north to south, and that accretion continued until early Carboniferous time (353.6 Ma).

## 7. Conclusions

- (1) The Mazongshan subduction–accretion mélange is characterized by a ‘block-in-matrix’ structure, the ‘blocks’ mainly consisting of serpentinized peridotite, basalt, gabbro, andesite, chert and seamount sediments in a matrix of turbidite and shale.
- (2) The Mazongshan complex evolved from a variety of sources and tectonic environments. The ophiolitic rocks that have an E-MORB geochemical signature formed with tholeiitic and alkaline basalts and diorites during initial intra-ocean subduction. The lithologies and geochemical characteristics of continental-arc lavas indicate formation in a relatively mature arc during the change from an initial immature oceanic arc to a mature continental arc.
- (3) The Mazongshan mélange contains two gabbro blocks that have U–Pb zircon ages of  $454.6 \pm 2.5$  and  $434.1 \pm 3.6$  Ma, and an andesite block with an age of  $451.3 \pm 3.5$  Ma; these isotopic ages indicate that the Mazongshan complex formed during Late Ordovician – early Silurian time. The age of the oldest rocks ( $454.6 \pm 2.5$  Ma) provides the time of initial accretion and tectonic emplacement after the Late Ordovician Epoch.
- (4) The age of the tuffaceous slate ( $353.6 \pm 5.1$  Ma) and of the youngest rocks ( $353.6 \pm 5.1$  Ma) indicates that the accretion continued until early Carboniferous time. The Mazongshan back-arc basin began to shrink as a consequence of N-wards subduction of the Palaeo-Asian Ocean during Late Ordovician – early Carboniferous time. Subsequently, it was accreted as a relict ophiolite into the accretionary orogen that we see today.

**Acknowledgements.** This study was funded by the National Natural Science Foundation of China (grant no. 41772107), the Geological Survey of China (grant no. DD20190370), the National Key Research and Development

Program of China (grant no. 2016YFC0601005) and the National Nonprofit Institute Research Grant of IGGE (grant no. AS2019Y01).

## References

- Anonymous** (1972) Ophiolites. *Geotimes* 17, 24–5.
- Ao SJ, Xiao WJ, Han CM, Li XH, Qu JF, Zhang JE, Guo QQ and Tian ZH** (2012) Cambrian to early Silurian ophiolite and accretionary processes in the Beishan collage, NW China: implications for the architecture of the Southern Altaids. *Geological Magazine* 149, 606–25.
- Ao SJ, Xiao WJ, Windley BF, Mao QG, Han CM, Zhang JE, Yang LK and Geng JZ** (2016) Paleozoic accretionary orogenesis in the eastern Beishan orogen: constraints from zircon U–Pb and  $40\text{Ar}/39\text{Ar}$  geochronology. *Gondwana Research* 30, 224–35.
- Brenan JM, Shaw HF and Ryerson FJ** (1995) Experimental evidence for the origin of lead enrichment in convergent-margin magmas. *Nature* 378, 54–6.
- Brown EH and Gehrels GE** (2007) Detrital zircon constraints on terrane ages and affinities and timing of orogenic events in the San Juan Islands and North Cascades, Washington. *Canadian Journal of Earth Sciences* 44, 1375–96.
- Castillo P, Solidum R and Punongbayan R** (2002) Origin of high field strength element enrichment in the Sulu Arc, southern Philippines, revisited. *Geology* 30, 707–10.
- Cawood PA, Kröner A, Collins WJ, Kusky TM, Mooney WD and Windley BF** (2009) Accretionary orogens through Earth history. In *Earth Accretionary Systems in Space and Time* (eds PA Cawood and A Kröner), pp. 1–36. Geological Society of London, Special Publication no. 318.
- Chen C, Xiu D, Pan ZL, Zhang H, Zhang JL, Li QZ and Zhuang SP** (2017) Early Paleozoic crustal extensional tectonic regime in the central part of Beishan Orogenic Belt: new evidence from geochronology and geochemistry of gabbro in Shibanzhong. *Acta Geologica Sinica* 91, 1661–73 (in Chinese with English abstract).
- Condie K** (2007) Accretionary orogens in space and time. In *4-D Framework of Continental Crust* (eds RD Hatcher Jr, MP Carlson, JH McBride and JR Martínez Catalán), pp. 145–58. Geological Society of America, Boulder, Memoir no. 200.
- Davidson JP and Arculus RJ** (2006) The significance of Phanerozoic arc magmatism in generating continental crust. In *Evolution and Differentiation of the Continental Crust* (eds M Brown and T Rushmer), pp. 135–72. Cambridge: Cambridge University Press.
- Davies JH and Stevenson DJ** (1992) Physical model of source region of subduction zone volcanics. *Journal of Geophysical Research: Solid Earth* 97, 2037–70.
- Degtyarev KE** (2011) Tectonic evolution of Early Paleozoic island-arc systems and continental crust formation in the Caledonides of Kazakhstan and the North Tien Shan. *Geotectonics* 45, 23–50.
- Dickinson WR and Gehrels GE** (2009) Use of U–Pb ages of detrital zircons to infer maximum depositional ages of strata: A test against a Colorado Plateau Mesozoic database. *Earth and Planetary Science Letters* 288, 115–25.
- Dilek Y and Furnes H** (2011) Ophiolite genesis and global tectonics: geochemical and tectonic fingerprinting of ancient oceanic lithosphere. *Geological Society of America Bulletin* 123, 387–411.
- Dilek Y and Furnes H** (2014) Ophiolites and their origins. *Elements* 10, 93–100.
- Ding JX, Han CM, Xiao WJ, Wang ZM and Yang XM** (2015) Geochemistry and U–Pb geochronology of tungsten deposit of Huaniushan island arc in the Beishan Orogenic Belt, and its geodynamic background. *Acta Petrologica Sinica* 31, 594–616 (in Chinese with English abstract).
- Elliott T, Plank T, Zindler A, White W and Bourdon B** (1997) Element transport from slab to volcanic front at the Mariana arc. *Journal of Geophysical Research: Solid Earth* 102, 14991–5019.
- Fliedner M and Klempner S** (2000) Crustal structure transition from oceanic arc to continental arc, Eastern Aleutian Islands and Alaska Peninsula. *Earth and Planetary Science Letters* 179, 567–79.
- Gangu Survey Institute** (2001) Geological Map of the Mazongshan Region, China, 1:250,000. No. 3 Geological Survey Team of the Gansu Bureau of Geology and Mineral Deposits (in Chinese).
- Gangu Survey Institute** (2008) Geological Map of the Mazongshan Region, China, 1:50,000. No. 3 Geological Survey Team of the Gansu Bureau of Geology and Mineral Deposits (in Chinese).

- Guo QQ, Xiao WJ, Hou QL, Windley BF, Han CM, Tian ZH and Song DF (2014) Construction of Late Devonian Dundunshan arc in the Beishan orogen and its implication for tectonics of southern Central Asian Orogenic Belt. *Lithos* **184–187**, 361–78.
- He ZY, Zhang ZM, Zong KQ, Xiang H, Chen XJ and Xia MJ (2014a) Zircon U–Pb and Hf isotopic studies of the Xingxingxia Complex from Eastern Tianshan (NW China): significance to the reconstruction and tectonics of the southern Central Asian Orogenic Belt. *Lithos* **190–191**, 485–99.
- He ZY, Zhang ZM, Zong KQ, Xiang H and Klemm R (2014b) Metamorphic P–T–t evolution of mafic HP granulites in the northeastern segment of the Tarim Craton (Dunhuang block): evidence for early Paleozoic continental subduction. *Lithos* **196–197**, 1–13.
- Hou QY, Wang Z, Liu JB, Wang J and Li DP (2012) Geochemistry characteristics and SHRIMP dating of Yueyashan ophiolite in Beishan orogen. *Geoscience* **26**, 1008–18 (in Chinese with English abstract).
- Hu XZ, Zhao GC, Hu XY, Liao YF and Cheng HF (2015) Geological characteristics, formation epoch and geotectonic significance of the Yueyashan ophiolitic tectonic mélange in the Beishan area, Inner Mongolia. *Geological Bulletin of China* **34**, 425–36 (in Chinese with English abstract).
- Isozaki Y (1996) Anatomy and genesis of a subduction-related orogen: a new view of geotectonic subdivision and evolution of the Japanese Islands. *Island Arc* **5**, 289–320.
- Jahn B-M, Wu F and Chen B (2000) Granitoids of the Central Asian Orogenic Belt and continental growth in the Phanerozoic. *Transactions of the Royal Society of Edinburgh: Earth Sciences* **91**, 181–93.
- Kröner A, Hegner E, Lehmann B, Heinhorst J, Wingate MTD, Liu DY and Ermelov P (2008) Palaeozoic arc magmatism in the Central Asian Orogenic Belt of Kazakhstan: SHRIMP zircon ages and whole-rock Nd isotopic systematics. *Journal of Asian Earth Sciences* **32**, 118–30.
- Kusky TM, Windley BF, Safonova I, Wakita K, Wakabayashi J, Polat A and Santosh M (2013) Recognition of ocean plate stratigraphy in accretionary orogens through Earth history: a record of 3.8 billion years of sea floor spreading, subduction, and accretion. *Gondwana Research* **24**, 501–47.
- Li XM, Yu JY, Wang GQ and Wu P (2012) Geochronology of Jijitaizi ophiolite in Beishan area, Gansu Province, and its geological significance. *Geological Bulletin of China* **31**, 2025–31 (in Chinese with English abstract).
- Liu YS, Hu ZC, Gao S, Günther D, Xu J, Gao CG and Chen HH (2008) In situ analysis of major and trace elements of anhydrous minerals by LA-ICP-MS without applying an internal standard. *Chemical Geology* **257**, 34–43.
- Ludwig KR (2000) *Users Manual for Isoplot/Ex: A Geochronological Toolkit for Microsoft Excel*. Berkeley Geochronology Center, Berkeley, Special Publication 1a, 53.
- Mao QG, Xiao WJ, Fang TH, Wang JB, Han CM, Sun M and Yuan C (2012) Late Ordovician to early Devonian adakites and Nb-enriched basalts in the Liuyuan area, Beishan, NW China: implications for early Paleozoic slab-melting and crustal growth in the southern Altaids. *Gondwana Research* **22**, 534–53.
- Mao QG, Xiao WJ, Windley BF, Han CM, Qu JF, Ao SJ, Zhang JE and Guo QQ (2011) The Liuyuan complex in the Beishan, NW China: a Carboniferous–Permian ophiolitic fore-arc sliver in the southern Altaids. *Geological Magazine* **149**, 483–506.
- Maruyama S (1997) Pacific-type orogeny revisited: Miyashiro-type orogeny proposed. *Island Arc* **6**, 91–120.
- Pearce JA (2008) Geochemical fingerprinting of oceanic basalts with applications to ophiolite classification and the search for Archean oceanic crust. *Lithos* **100**, 14–48.
- Pearce JA (2014) Geochemical fingerprinting of the Earth's oldest rocks. *Geology* **42**, 175–76.
- Reagan MK, Ishizuka O, Stern RJ, Kelley KA, Ohara Y, Blichert-Toft J, Bloomer SH, Cash J, Fryer P, Hanan BB, Hickey-Vargas R, Ishii T, Kimura J-I, Peate DW, Rowe MC and Woods M (2010) Fore-arc basalts and subduction initiation in the Izu-Bonin-Mariana system. *Geochemistry, Geophysics, Geosystems* **11**, published online 6 March 2010, doi: [10.1029/2009GC002871](https://doi.org/10.1029/2009GC002871).
- Ren BC, He SP, Yao WG and Fu LP (2001) Rb–Sr isotope age Niujuanzi ophiolite and its tectonic significance in Beishan district, Gansu. *Northwestern Geology* **34**, 21–7 (in Chinese with English abstract).
- Safonova IY, Perfilova AA, Obut OT, Savinsky IA, Chyorny RI, Petrenko NA, Gurova AV, Kotler PD, Khromykh SV, Krivonogov SK and Maruyama S (2019) The Itmurundy accretionary complex, Northern Balkhash area: geological structure, stratigraphy and tectonic origin. *Russian Journal of Pacific Geology* **13**, 283–96.
- Safonova IY and Santosh M (2014) Accretionary complexes in the Asia-Pacific region: tracing archives of ocean plate stratigraphy and tracking mantle plumes. *Gondwana Research* **25**, 126–58.
- Safonova IY, Seltmann R, Kröner A, Gladkochub D, Kim J-Y, Schulmann K, Xiao W, Komiya T and Sun M (2011) A new concept of continental construction in the Central Asian Orogenic Belt: (compared to actualistic examples from the Western Pacific). *Episodes* **34**, 1–10.
- Schulmann K and Paterson S (2011) Geodynamics of Asian continental growth. *Nature Geoscience* **4**, 827–29.
- Şengör AMC, Natal'in BA and Burtman VS (1993) Evolution of the Altaid tectonic collage and Palaeozoic crustal growth in Eurasia. *Nature* **364**, 299–307.
- Şengör AMC, Natal'in BA, Sunal G and Voo RVD (2014) A new look at the Altaids: a super-orogenic complex in northern and central Asia as a factory of continental crust. Part I: geological data compilation (exclusive of palaeomagnetic observations). *Austrian Journal of Earth Sciences* **107**, 169–232.
- Shervais JW (1982) Ti–V plots and the petrogenesis of modern and ophiolitic lavas. *Earth and Planetary Science Letters* **59**, 101–18.
- Shervais JW (2001) Birth, death, and resurrection: The life cycle of suprasubduction zone ophiolites. *Geochemistry, Geophysics, Geosystems* **2**, 2000GC000080.
- Shi YR, Zhang W, Kröner A, Li LL and Jian P (2018) Cambrian ophiolite complexes in the Beishan area, China, southern margin of the Central Asian Orogenic Belt. *Journal of Asian Earth Sciences* **153**, 193–205.
- Shu LS, Wang B and Zhu WB (2007) Age of radiolarian fossils from the Heiyingshan Ophiolitic Mélange, Southern Tianshan Belt, NW China, and its tectonic significance. *Acta Geologica Sinica* **81**, 1161–70.
- Song DF, Xiao WJ, Han CM, Li JL, Qu JF, Guo QQ, Lin LN and Wang ZM (2013a) Progressive accretionary tectonics of the Beishan orogenic collage, southern Altaids: insights from zircon U–Pb and Hf isotopic data of high-grade complexes. *Precambrian Research* **227**, 368–88.
- Song DF, Xiao WJ, Han CM and Tian ZH (2013b) Geochronological and geochemical study of gneiss–schist complexes and associated granitoids, Beishan Orogen, southern Altaids. *International Geology Review* **55**, 1705–27.
- Song DF, Xiao WJ, Han CM and Tian ZH (2014) Polyphase deformation of a Paleozoic forearc–arc complex in the Beishan orogen, NW China. *Tectonophysics* **632**, 224–43.
- Song DF, Xiao WJ, Han CM, Tian ZH and Wang ZM (2013c) Provenance of metasedimentary rocks from the Beishan orogenic collage, southern Altaids: constraints from detrital zircon U–Pb and Hf isotopic data. *Gondwana Research* **24**, 1127–51.
- Song DF, Xiao WJ, Windley BF, Han CM and Tian ZH (2015) A Paleozoic Japan-type subduction-accretion system in the Beishan orogenic collage, southern Central Asian Orogenic Belt. *Lithos* **224–225**, 195–213.
- Stolz AJ, Jochum KP, Spettel B and Hofmann AW (1996) Fluid- and melt-related enrichment in the sub-arc mantle: Evidence from Nb/Ta variations in island-arc basalts. *Geology* **24**, 586–90.
- Sun S-S and McDonough WF (1989) Chemical and isotopic systematics of oceanic basalts: implications for mantle composition and source processes. In *Magmatism in the Ocean Basins* (eds AD Saunders and MJ Norry), pp. 313–45. Geological Society of London, Special Publication no. 42.
- Tian ZH, Xiao WJ, Windley BF, Lin LN, Han CM, Zhang JE, Wan B, Ao SJ, Song DF and Feng JY (2014) Structure, age, and tectonic development of the Huoshishan–Niujuanzi ophiolitic mélange, Beishan, southernmost Altaids. *Gondwana Research* **25**, 820–41.
- Tian ZH, Xiao WJ, Windley BF, Zhang JE, Zhang ZY and Song DF (2016) Carboniferous rifted arcs leading to an archipelago of multiple arcs in the Beishan–Tianshan orogenic collages (NW China). *International Journal of Earth Sciences* **106**, 2319–42.
- Wakabayashi J (2011) Mélanges of the Franciscan Complex, California: Diverse structural settings, evidence for sedimentary mixing, and their connection to subduction processes. In *Mélanges: Processes of Formation and Societal Significance* (eds J Wakabayashi and Y Dilek), pp. 117–41. Geological Society of America, Boulder, Special Paper no. 480.

- Wakita K, Pubellier M and Windley B** (2013) Tectonic processes, from rifting to collision via subduction, in SE Asia and the western Pacific: a key to understanding the architecture of the Central Asian Orogenic Belt. *Lithosphere* **5**, 265–76.
- Wan TF and Zhu H** (2011) Chinese continental blocks in global Paleocentennial reconstruction during Paleozoic and Mesozoic. *Acta Geologica Sinica (English Edition)* **85**, 581–97.
- Wang GQ, Li XM, Xu XY and Wu P** (2014) Zircon U–Pb chronological study of the Hongshishan ophiolite in the Beishan area and their tectonic significance. *Acta Petrologica Sinica* **30**, 1685–94 (in Chinese with English abstract).
- Wang GQ, Li XM, Xu XY, Yu JY, Guo L, Yan QJ, Ji B and Wu P** (2016) Geochemistry of Gongpoquan Group in the Beishan area, Gansu Province: constraints on petrogenesis and tectonic setting. *Acta Geologica Sinica* **90**, 2603–19.
- Wang SD, Zhang KX, Song BW, Li SC, Li JX, Yu JY and Bu JJ** (2018a) Detrital Zircon U–Pb geochronology from greywackes in the Niujuanzi Ophiolitic Mélange, Beishan Area, NW China: provenance and tectonic implications. *Journal of Earth Science* **29**, 103–13.
- Wang SD, Zhang KX, Song BW, Li SC, Li M and Zhou J** (2017) Geochronology and geochemistry of the Niujuanzi ophiolitic mélange, Gansu Province, NW China: implications for tectonic evolution of the Beishan Orogenic Collage. *International Journal of Earth Sciences* **107**, 269–89.
- Wang XY, Yuan C, Zhang YY, Long XP, Sun M, Wang LX, Soldner J and Lin ZF** (2018b) S-type granite from the Gongpoquan arc in the Beishan Orogenic Collage, southern Altaids: implications for the tectonic transition. *Journal of Asian Earth Sciences* **153**, 206–22.
- Wilhem C, Windley BF and Stampfli GM** (2012) The Altaids of Central Asia: a tectonic and evolutionary innovative review. *Earth-Science Reviews* **113**, 303–41.
- Winchester JA and Floyd PA** (1977) Geochemical discrimination of different magma series and their differentiation products using immobile elements. *Chemical Geology* **20**, 325–43.
- Windley B and Xiao WJ** (2018) Ridge subduction and slab windows in the Central Asian Orogenic Belt: tectonic implications for the evolution of an accretionary orogen. *Gondwana Research* **61**, 73–87.
- Windley BF** (1992) Proterozoic collisional and accretionary orogens. In *Proterozoic Crustal Evolution* (ed. KC Condie), pp. 419–46. Elsevier: Amsterdam.
- Windley BF, Alexeiev D, Xiao WJ, Kröner A and Badarch G** (2007) Tectonic models for accretion of the Central Asian Orogenic Belt. *Journal of the Geological Society, London* **164**, 31–47.
- Wood DA** (1980) The application of a Th–Hf–Ta diagram to problems of tectonomagmatic classification. *Earth and Planetary Science Letters* **50**, 1–30.
- Wu P, Wang GQ, Li XM, Yu JY and Kang L** (2012) The age of Niujuanzi ophiolite in Beishan area of Gansu Province and its geological significance. *Geological Bulletin of China* **31**, 2032–37 (in Chinese with English abstract).
- Xiao QH, Li TD, Pan GT, Lu SN, Ding XZ, Deng JF, Feng YM, Liu Y, Kou CH and Yang LL** (2016) Petrologic ideas for identification of ocean-continent transition: recognition of intra-oceanic arc and initial subduction. *Geology in China* **43**, 721–37 (in Chinese with English abstract).
- Xiao WJ, Han CM, Liu W, Wan B, Zhang JE, Ao SJ, Zhang ZY, Song DF, Tian ZH and Luo J** (2014) How many sutures in the southern Central Asian Orogenic Belt: insights from East Xinjiang–West Gansu (NW China)? *Geoscience Frontiers* **5**, 525–36.
- Xiao WJ, Han CM, Yuan C, Sun M, Zhao GC and Shan YH** (2010a) Transitions among Mariana-, Japan-, Cordillera- and Alaska-type arc systems and their final juxtapositions leading to accretionary and collisional orogenesis. In *The Evolving Continents: Understanding Processes of Continental Growth* (eds TM Kusky, M-G Zhai and W Xiao), pp. 35–53. Geological Society of London, Special Publication no. 338.
- Xiao WJ, Huang BC, Han CM, Sun S and Li JL** (2010b) A review of the western part of the Altaids: a key to understanding the architecture of accretionary orogens. *Gondwana Research* **18**, 253–73.
- Xiao WJ, Mao QG, Windley BF, Han CM, Qu JF, Zhang JE, Ao SJ, Guo QQ, Cleven NR, Lin SF, Shan YH and Li JL** (2010c) Paleozoic multiple accretionary and collisional processes of the Beishan orogenic collage. *American Journal of Science* **310**, 1553–94.
- Xiao WJ, Windley BF, Badarch G, Sun S, Li JL, Qin KZ and Wang ZH** (2004) Paleozoic accretionary and convergent tectonics of the southern Altaids: implications for the growth of Central Asia. *Journal of the Geological Society, London* **161**, 339–42.
- Xiao WJ, Windley BF, Hao J and Zhai MG** (2003) Accretion leading to collision and the Permian Solonker suture, Inner Mongolia, China: termination of the central Asian orogenic belt. *Tectonics* **22**, 1–15.
- Xiao WJ, Windley BF, Sun S, Li JL, Huang BC, Han CM, Yuan C, Sun M and Chen HL** (2015) A tale of amalgamation of three Permo-Triassic collage systems in Central Asia: oroclines, sutures, and terminal accretion. *Annual Review of Earth and Planetary Sciences* **43**, 477–507.
- Xiao WJ, Windley BF, Yuan C, Sun M, Han CM, Lin SF, Chen HL, Yan QR, Liu DY, Qin KZ, Li JL and Sun S** (2009) Paleozoic multiple subduction-accretion process of the southern Altaids. *American Journal of Science* **309**, 221–70.
- Yu FS, Li JB and Wang T** (2006) The U–Pb isotopic age of zircon from Hongliuhe ophiolites in East Tianshan mountains, Northwest China. *Acta Geoscientica Sinica* **27**, 213–16 (in Chinese with English abstract).
- Zhang KX, Feng QL, Song BW, Zhang ZY, Wang YH, Pan GT, Lu SN, Zhao XM and Xing GF** (2014a) Non-Smithian strata in the orogen. *Earth Science Frontiers (China University of Geosciences (Beijing); Peking University)* **21**, 36–47 (in Chinese with English abstract).
- Zhang YY and Guo ZJ** (2008) Accurate constraint on formation and emplacement age of Hongliuhe ophiolite, boundary region between Xinjiang and Gansu Provinces and its tectonic implications. *Acta Petrologica Sinica* **24**, 803–9 (in Chinese with English abstract).
- Zhang KX, He WH, Xu YD, Luo MS, Song BW, Kou XH and Xing ZY** (2018) *Explanatory Note of the Sedimentary Tectonic Map of China (1:2 500 000)*. Beijing, China: Geological Publishing House.
- Zhang KX, He WH, Xu YD, Luo MS, Song BW, Kou XH, Zhang ZY, Xiao QH and Pan GT** (2016) Palaeogeographic distribution and tectonic evolution of OPS in China. *Earth Science Frontiers (China University of Geosciences (Beijing); Peking University)* **23**, 24–30 (in Chinese with English abstract).
- Zhang KX, He WH, Xu YD, Luo MS, Song BW, Zhang ZY, Pan GT, Wang YH, Zhao XM and Xing GF** (2014b) Subdivision and identification of sedimentary tectonic facies. *Earth Science—Journal of China University of Geosciences* **39**, 915–28 (in Chinese with English abstract).
- Zhang KX, Pan GT, He WH, Xiao QH, Xu Y-D, Zhang Z, Lu S, Deng J, Feng Y, Li J, Zhao X, Xing G, Wang Y, Yin F, Hao G, Zhang C, Zhang J and Gong Y** (2015) New division of tectonic-strata super-region in China. *Earth Science—Journal of China University of Geosciences* **40**, 206–33 (in Chinese with English abstract).
- Zheng RG, Li JY and Xiao WJ** (2019) Mid-Paleozoic ridge subduction in the Central Beishan of the southern Altaids: evidence from geochemical, Sr–Nd and zircon U–Pb–Hf–O isotopic data of Gongpoquan volcanic rocks. *Journal of the Geological Society, London* **176**, 755–70.
- Zheng RG, Wu TR, Zhang W, Xu C and Meng QP** (2013) Late Paleozoic subduction system in the southern Central Asian Orogenic Belt: evidences from geochronology and geochemistry of the Xiaohuangshan ophiolite in the Beishan orogenic belt. *Journal of Asian Earth Sciences* **62**, 463–75.
- Zheng RG, Xiao WJ, Li JY, Wu TR and Zhang W** (2018) A Silurian-early Devonian slab window in the southern Central Asian Orogenic Belt: evidence from high-Mg diorites, adakites and granitoids in the western Central Beishan region, NW China. *Journal of Asian Earth Sciences* **153**, 75–99.
- Zheng YF** (2012) Metamorphic chemical geodynamics in continental subduction zones. *Chemical Geology* **328**, 5–48.
- Zheng YF** (2019) Subduction zone geochemistry. *Geoscience Frontiers* **10**, 1223–54.
- Zuo GC, Jin SQ and Feng TQ** (1994) Conodonts were found in the Gansu Province. *Regional Geology of China* **2**, 185 (in Chinese with English abstract).
- Zuo GC, Liu YK and Liu CY** (2003) Framework and evolution of the tectonic structure in Beishan area across Gansu Province, Xinjiang Autonomous region and Inner Mongolia Autonomous region. *Acta Geologica Gansu* **12**, 1–15 (in Chinese with English abstract).